

Internal Structure and Apsidal Motions of Polytropic Stars in Close Binaries

Fedir V. Sirotkin & Woong-Tae Kim

sirotkin.f.v@gmail.com, wkim@astro.snu.ac.kr

Department of Physics and Astronomy, FPRD, Seoul National University, Seoul, 151-742, South Korea

ABSTRACT

We consider a synchronized, circular-orbit binary consisting of a polytrope with index n and a point-mass object, and use a self-consistent field method to construct the equilibrium structure of the polytrope under rotational and tidal perturbations. Our self-consistent field method is distinct from others in that the equilibrium orbital angular velocity is calculated automatically rather than being prescribed, which is crucial for obtaining apsidal motion rates accurately. We find that the centrifugal and tidal forces make perturbed stars more centrally condensed and larger in size. For $n = 1.5$ polytropes with fixed entropy, the enhancement factor in stellar radii is about 23% and 4 – 8% for $\mu = 1$ and $\sim 0.1 - 0.9$, respectively, where μ is the fractional mass of the polytrope relative to the total. The centrifugal force dominates the tidal force in determining the equilibrium structure provided $\mu \gtrsim 0.13 - 0.14$ for $n \gtrsim 1.5$. The shape and size of rotationally- and tidally-perturbed polytropes are well described by the corresponding Roche models as long as $n \gtrsim 2$. The apsidal motion rates calculated for circular-orbit binaries under the equilibrium tide condition agree well with the predictions of the classical formula only when the rotational and tidal perturbations are weak. When the perturbations are strong as in critical configurations, the classical theory underestimates the real apsidal motion rates by as much as 50% for $n = 1.5$ polytropes, although the discrepancy becomes smaller as n increases. For practical uses, we provide fitting formulae for the density concentration, volume radius, coefficient of the mass-radius relation, moment of inertia, spin angular momentum, critical rotation parameter, effective internal structure constant, etc., as functions of μ and the perturbation parameters.

Subject headings: binaries: close – method: numerical – stars: interiors – stars: rotation

1. Introduction

Binary systems are an ideal laboratory for the study of stellar astrophysics. They not only provide direct information on stellar mass, radius, and luminosity, which are all fundamental for the theory of stellar evolution, but also allow to probe stellar structures by measuring apsidal motions

(e.g., Eggleton 2006; Giménez 2007). Since tidal forces from a star in a binary system are likely to affect the rotation rate and internal structure of the other component, one expects that the stellar quantities such as radius and effective temperature of binary stars may differ from those of single stars, as confirmed by observations (e.g., Malkov 2003, 2007; Ribas 2006). While the literature abounds with studies on the rotational and tidal distortions of stars, most of the studies are either approximate or based on prescribed rotation profiles, as detailed below. In this work, we employ a fully self-consistent method to investigate the quantitative effects of centrifugal and tidal forces on equilibrium polytropes in synchronously-rotating, circular-orbit binaries.

Finding equilibrium configurations of polytropic stars under rotational (and/or tidal) distortion dates back to Chandrasekhar (1933a,b,c) who used a perturbation theory in which an equilibrium density distribution was regarded as a small departure from a corresponding unperturbed Lane-Emden function. Chandrasekhar considered only first-order terms in the rotation parameter ν (see eq. [17] for definition), corresponding to slow rotation. Later, this perturbation method was extended to include terms of second order (Anand 1968; Geroyannis et al. 1979) and third order (Geroyannis & Valvi 1984). The first-order perturbation theory was further refined by Linnell (1977, 1981) who retained the first-order terms in the potential expansion, while allowing for large deformation of the equilibrium configurations from the unperturbed polytropes. More recently, Geroyannis (1988) showed that the first-order perturbation theory combined with “complex Lane-Emden functions” beyond their first roots gives much improved results for rotating polytropes.

Kippenhahn & Thomas (1970) used a quasi-spherical method in which (1) the rotation velocity is assumed to be spherically symmetric rather than being cylindrically symmetric and (2) only the radial component of the centrifugal force is considered in the force balance; these assumptions make rotating stars essentially spherical. Recently, Arbutina (2009) used a similar method to study the change of the total angular momentum due to tidal perturbations and the associated tidal instability. While the quasi-spherical method was able to handle the effects of rotation on stellar evolution in a very simplified way, it readily fails when the stellar shape becomes quite non-spherical.

To study the internal structure of binary stars, Kopal (1972) constructed the Roche model where the actual equipotential surfaces of distorted stars are approximated by the corresponding Roche potentials of two point-mass stars (see also Kopal 1978; Mohan & Singh 1978; Mohan & Saxena 1983; Mohan et al. 1990, 1992, 1997). While the Roche model is a good approximation for stars with very high central concentration, it assumes Keplerian orbits and thus cannot give any clue to the apsidal motions of binary stars.

On the other hand, Monaghan & Roxburgh (1965) developed a so-called “double-approximation method” in which a distorted star is divided into two parts: a core containing most of the stellar material and a non-self-gravitating, low-density envelope. While the envelope is highly susceptible to applied centrifugal and tidal forces, the distortion of the core is assumed to be small even in the case of critical rotation. Depending on the method to calculate the distortion of the core,

the double-approximation method has several different branches: Monaghan & Roxburgh (1965), Jackson (1970), Durney & Roxburgh (1970), and Naylor & Anand (1972a,b) used first-order perturbation theory of Chandrasekhar (1933a); Martin (1970) and Singh & Singh (1984) included terms up to of second order; Meynet & Maeder (1997) and Lal et al. (2006) employed the quasi-spherical method.

Although the aforementioned work have improved our understanding of the rotational and tidal effects on stellar structure, these are only approximate and do not yield accurate results when the perturbations are rather strong. It was James (1964) who first sought for direct numerical solutions for rotationally distorted polytropes without any assumption. By expanding the potential-density pairs in Legendre polynomials up to of tenth order and integrating a set of the resulting ordinary differential equations *simultaneously*, James (1964) obtained solutions, with truncation errors less than 0.2%, for rotating polytropes. On the other hand, Ostriker & Mark (1968) introduced a self-consistent field (SCF) method that provides a concise, accurate, and very efficient computation scheme. In the SCF method, the equilibrium density distribution is found by solving the Poisson equation as well as the equilibrium condition, *alternatively* and *iteratively*, for the potential-density pairs. The SCF method is so powerful that it has been applied to various problems including the structure of rotating stars (Ostriker & Bodenheimer 1968; Mark 1968; Clement 1974; Stahler 1983a,b; Hachisu 1986a) and galactic dynamics of collisionless systems (Hernquist & Ostriker 1992; Hernquist et al. 1995; Weinberg 1999; Gnedin 2003). Recently, MacGregor et al. (2007) used a modified version of the SCF method to construct stellar models for differentially-rotating, low-mass, main-sequence stars with a realistic equation of state (see also Jackson et al. 2005).

While most SCF methods for distorted stars are two-dimensional under rotational symmetry, Hachisu (1986b) formulated a three-dimensional SCF method to calculate structures of rotating multi-body systems in which tidal effects are implicitly included. He showed numerically that there is an equilibrium sequence along which an ellipsoid takes on a dumbbell-like shape as the angular momentum of the whole system increases, eventually separating into a binary. Although Hachisu (1986b) calculated the density structures and shapes of multi-body systems, these are for equal-mass objects (owing to the imposed azimuthal symmetry) with a few prescribed laws for spin and orbital angular velocities. Later, Hachisu et al. (1986a,b) generalized the method to allow for unequal-mass binaries, but the rotational velocity is still given externally rather than being calculated self-consistently, which makes it impossible to obtain information on apsidal motions.

Finding accurate internal structures of distorted stars in close binary systems are also of great importance in testing the classical theory of apsidal motions. Apsidal motions arise when the gravitational force due to a star is different from that of a Newtonian point-mass. The chief cause of perturbations to Keplerian orbits is the rotational and tidal distortions that make the figures of binary stars deviate from spherical symmetry. Also, the separate or combined effects of the general relativistic correction, the presence of a third body, and non-equilibrium tides can be also non-negligible (see recent review of Giménez 2007). For binary stars in near-circular motions, Russell (1928) showed that the advance rate, $\dot{\omega}$, of the apsidal line due to the tidal and rotational distortion

of star I with mass M_1 caused by the attraction of star II with mass M_2 is given by

$$\frac{\dot{\varpi}}{\Omega_K} = k_2 \left(\frac{R_1}{A} \right)^5 \left(1 + 7 \frac{M_2}{M_1} \right), \quad (1)$$

where $\Omega_K = (G[M_1 + M_2]/A^3)^{1/2}$ is the Keplerian angular velocity, R_1 is the mean radius of star I, A is the orbital separation, and k_2 is the dimensionless apsidal motion constant. Through more rigorous, first-order perturbation analyses, Cowling (1938) and Stern (1939) generalized equation (1) to make it applicable to binaries with eccentric orbits, which has been widely used to estimate the degree of the internal density concentration via k_2 from observations.

However, the classical formulae of Russell (1928), Cowling (1938), and Stern (1939) have two limitations. First, by ignoring the cross terms of spherical harmonics in expanding equipotential surfaces, they are valid in a strict sense only when the tidal and rotational distortions are weak. Second, by assuming an instantaneous adjustment of a star to time-dependent tidal force, they fail when the orbital period is shorter than the oscillation periods of tidally excited modes inside the perturbed star. Quataert et al. (1996) and Smeyers & Willems (2001) relaxed the second limitation to study the effects of dynamical and resonance tides (still based on a linear perturbation theory), finding that the classical formulae are accurate as long as the ratio of the modal to orbital frequencies is less than about 10 (see also Claret & Willems 2003). The validity of the classical formulae is nonetheless questionable for close binaries, especially in the critical configurations, where the distortion of a stellar shape is large enough for nonlinear terms to be non-negligible.

Despite a long history of research, therefore, studies are still lacking as to how the stellar structure, shape, size, etc. of a distorted star as well as its apsidal motion rate in a close binary system vary with the fundamental parameters such as the mass ratio and orbital distance. More specifically, how good are the approximate methods described above for highly distorted stars? What is the relative role of tidal force to centrifugal force in increasing the central density concentration? Can the classical theory of apsidal motions based on perturbation analyses be accurately applied even to critical configurations? To address these questions, we in this work consider a circular-orbit binary in which two components are modeled as a polytrope and a point-mass, respectively, and calculate the equilibrium structure of the polytrope using an SCF method. The binary is assumed to be in spin-orbit synchronization, so that the tide is independent of time. As explained below, two salient features of our SCF method compared to those in the previous studies are that the former considers only the polytropic component in density computation, while explicitly including the tidal force from its companion as a fixed gravitational potential, and that the orbital velocity indispensable for calculating the apsidal motion rates is now obtained self-consistently from the equilibrium condition.

The organization of this paper is as follows. In §2, we describe our implementation of the SCF method to find the equilibrium structure of a synchronously rotating binary component. In §3, we first present the numerical solutions for unperturbed polytropes and uniformly-rotating polytropes and compare them with the published results. We then turn to the solutions for both rotationally-

and tidally-distorted polytropes, and give detailed quantitative results on the changes of internal structures as well as on the parameters describing critical configurations. Using the self-consistent solutions of perturbed polytropes, we test the classical theory of apsidal motions in §4. Finally in §5, we summarize our results and discuss the astronomical implication of our work.

2. Formulation

2.1. Basic Equations

In this paper we use an SCF method to study the equilibrium structure of a self-gravitating star under the external gravitational force from a companion in a close binary system. We assume that two stars revolve in circular orbits with constant angular speed Ω and orbital separation A , so that the tidal force is stationary. We further assume that a star in question with mass M_1 and volume radius R_1 (hereafter star I), composed of inviscid polytropic gas without magnetic fields, rotates rigidly and synchronously with the orbital motion. For simplicity, we treat the companion star (hereafter star II) as a point mass with mass M_2 . We work in a rotating Cartesian frame at Ω whose origin lies at the center of mass of star I. Figure 1 schematically illustrates the binary configuration and the coordinate system in which the x -axis points toward star II located at $(x, y, z) = (A, 0, 0)$ and the z -axis is perpendicular to the orbital plane. Star I is distorted rotationally and tidally, and has a polar radius R_p and an equatorial radius R_e along the positive x -axis. We assume for computational convenience that all the substance of star I is contained within a sphere with radius R_L , the distance to the inner Lagrange point from the origin.

The equation of hydrostatic equilibrium then takes the form

$$\frac{\nabla P}{\rho} + \nabla \Phi = 0, \quad (2)$$

where P is the pressure, ρ is the density, and Φ is the effective potential defined by

$$\Phi = \Phi_\Omega + \Phi_* + \Phi_g. \quad (3)$$

In equation (3), Φ_Ω is the centrifugal potential

$$\Phi_\Omega = -\frac{\Omega^2}{2}\{[x - A(1 - \mu)]^2 + y^2\}, \quad (4)$$

with $\mu = M_1/(M_1 + M_2)$ being the mass fraction of star I, Φ_* is the gravitational potential from star II

$$\Phi_* = -\frac{GM_2}{\sqrt{(x - A)^2 + y^2 + z^2}}, \quad (5)$$

and Φ_g is the self-gravitational potential of star I that satisfies the Poisson equation

$$\nabla^2 \Phi_g = 4\pi G\rho. \quad (6)$$

The proper boundary conditions on Φ_g are that Φ_g and its first derivatives should behave well at $r = (x^2 + y^2 + z^2)^{1/2} \rightarrow 0$ and $r \rightarrow \infty$, and should be continuous on the surface of a polytrope. These boundary conditions are automatically satisfied when we use the integral representation of the Poisson equation in §2.3 below.

We assume that the matter of star I obeys a polytropic relation

$$P = K\rho^{1+1/n}, \quad (7)$$

with the pressure constant K and the polytropic index n . Equation (2) is then integrated to yield

$$\Phi + (n + 1)K\rho^{1/n} = \Phi_s, \quad (8)$$

where Φ_s is the potential on the surface of star I with vanishing density. An equilibrium condition for star II is simply

$$\Omega^2 = \frac{1}{\mu A} \frac{\partial \Phi_g}{\partial x} \Big|_{\mathbf{x}=(A,0,0)}, \quad (9)$$

which must be checked a posteriori.

Following the convention, we introduce the dimensionless coordinates $\boldsymbol{\xi} = (\xi, \eta, \zeta) \equiv (x, y, z)/\alpha$, where

$$\alpha = \left[\frac{(n + 1)K}{4\pi G} \rho_c^{1/n-1} \right]^{1/2}. \quad (10)$$

We also define the generalized Lane-Emden function Θ through

$$\rho = \rho_c \Theta^n, \quad (11)$$

where the central density ρ_c is given by

$$\rho_c = \frac{M_1}{\alpha^3 \int \Theta^n d^3 \boldsymbol{\xi}}. \quad (12)$$

The equilibrium condition (8) then becomes

$$\Theta = \Psi_s - \Psi, \quad (13)$$

where $\Psi \equiv \Phi/([n + 1]K\rho_c^{1/n})$ and Ψ_s is the value of Ψ on the surface of star I.

In dimensionless forms, equations (4)-(6) and (9) read

$$\Psi_\Omega = -\frac{\nu}{4} \{ [\xi - \nu(1 - \mu)]^2 + \eta^2 \} \quad (14)$$

$$\Psi_* = -\frac{\nu}{2} \left(\frac{\Omega_K}{\Omega} \right)^2 \frac{\nu^3(1 - \mu)}{\sqrt{(\xi - \nu)^2 + \eta^2 + \zeta^2}}, \quad (15)$$

and

$$\tilde{\nabla}^2 \Psi_g = \Theta^n, \quad (16)$$

where $\tilde{\nabla}$ denotes a dimensionless derivative with respect to ξ . In equations (14) and (15), $\Omega_K^2 = G(M_1 + M_2)/A^3$ is the Keplerian angular velocity, $\nu \equiv A/\alpha$ is the dimensionless orbital distance, and v is the dimensionless angular velocity defined by

$$v \equiv \frac{\Omega^2}{2\pi G \rho_c} = \left(\frac{\Omega}{\Omega_K} \right)^2 \frac{\int \Theta^n d^3 \xi}{2\pi \mu \nu^3} \quad (17)$$

which is a measure of the amplitude of rotational perturbations (e.g., Chandrasekhar 1933b). It is sometimes useful to measure the degree of rotational perturbations in terms of the mean density $\bar{\rho} \equiv 3M_1/(4\pi R_1^3)$ as

$$\lambda \equiv \frac{\Omega^2}{2\pi G \bar{\rho}} = \frac{2\Omega^2 R_1^3}{3GM_1}, \quad (18)$$

(e.g., Stothers 1974; Claret 1999).

Because of tidal and rotational distortions, the orbital motions of close binary stars are different from purely Keplerian ones. For binaries in spin-orbit synchronization, the angular velocity is naturally constrained by equation (9), or its dimensionless form

$$\left(\frac{\Omega}{\Omega_K} \right)^2 = \frac{4\pi \nu^2}{\int \Theta^n d^3 \xi} \frac{\partial \Psi_g}{\partial \xi} \Bigg|_{\xi=(\nu,0,0)}. \quad (19)$$

However, it turned out in our SCF method that Ω/Ω_K calculated from equation (19) was too small and varied too much to give converged results at the very early stage of iterations. Instead, we empirically found that the condition

$$\left(\frac{\Omega}{\Omega_K} \right)^2 = 1 + \frac{1}{\nu(1-\mu)} \frac{\partial \Psi_g}{\partial \xi} \Bigg|_{(\xi,\eta,\zeta)=0}, \quad (20)$$

corresponding to a vanishingly-small pressure gradient at the center of mass of star I, allows the solutions to converge rapidly, and is in fact very similar to equation (19) when an equilibrium is achieved. In practice, therefore, we first use equation (20) to update Ω until a temporary convergence is made, and then switch to equation (19) to obtain the desired equilibrium solutions.

To check the accuracy of equilibrium configurations that we construct, we use the virial parameter ϵ defined by

$$\epsilon = \left| \frac{2T + 3 \int P dV + W}{W} \right|, \quad (21)$$

where $T = \frac{1}{2}\Omega^2 M_2 A^2 \mu^2 - \int \rho \Phi_\Omega d^3 x$ is the total kinetic energy and $W = \int (\Phi_g + \Phi_*) \rho d^3 x$ is the total gravitational potential energy.

2.2. Structure Parameters

A polytrope distorted by tidal and centrifugal forces in general has different radii in the equatorial and polar directions. To measure its size, we use the volume radius

$$R_1 = \alpha \xi_1 \equiv \left(\frac{3V}{4\pi} \right)^{1/3}, \quad (22)$$

where V denotes the volume enclosed by the isodensity surface with $\Theta = 0$. Note that in the absence of perturbing forces, ξ_1 is equal to the first zero of the Lane-Emden functions for unperturbed polytropes with $n < 5$ (e.g., Chandrasekhar 1939).

Substituting equation (12) into equation (10) and eliminating α in the resulting equation by use of equation (22) yield the mass-radius relation

$$K = N_n G M_1^{(n-1)/n} R_1^{(3-n)/n}, \quad (23)$$

where N_n denotes the numerical coefficient

$$N_n = \frac{4\pi \xi_1^{(n-3)/n}}{(n+1)} \left(\int \Theta^n d^3\xi \right)^{(1-n)/n}. \quad (24)$$

We note that equation (23) holds also for unperturbed polytropes, but with different values of N_n .

To characterize the degree of the mass concentration toward the center, we use

$$\frac{\rho_c}{\bar{\rho}} = \frac{4\pi \xi_1^3}{3 \int \Theta^n d^3\xi}. \quad (25)$$

The dimensionless moment of inertia of star I about the z -axis is defined by

$$I = \frac{1}{\alpha^5 \rho_c} \int \rho (x^2 + y^2) d^3x. \quad (26)$$

Finally, the total angular momentum of star I is given by

$$J_1 = -\frac{2}{\Omega} \int \rho \Phi_\Omega d^3x = J_{\text{orb}} + J_{\text{spin}}, \quad (27)$$

where $J_{\text{orb}} = \Omega M_1 A^2 (1 - \mu)^2$ and $J_{\text{spin}} = \Omega \int \rho (x^2 + y^2) d^3x = \alpha^5 \rho_c \Omega I$ are the orbital and spin angular momenta of star I, respectively. We will study in the next section the dependences of ξ_1 , N_n , $\rho_c/\bar{\rho}$, I , and $J_{\text{spin}}/J_{\text{orb}}$ upon the strength of centrifugal and tidal forces.

2.3. Expansion of Density-Potential Pair

For given values of n , μ , and ν , equations (13)-(16) constitute a closed set of equations for the equilibrium density Θ^n ; the rotation parameter v is related to the dimensionless angular velocity

Ω/Ω_K through equation (17) and Ω/Ω_K is constrained by equation (19) for binaries in spin-orbit synchronization. In an SCF method, the density and the potential are updated alternately and iteratively in such a way that at the i -th stage of iteration, equations (14)-(16) are used to obtain the potential Ψ_i from Θ_i , which is then substituted in equation (13) to yield Θ_{i+1} for the next iteration stage (Ostriker & Mark 1968).

We solve equation (16) using a multipole expansion technique in the region of space bounded by a sphere with radius R_L . For this, it is convenient to set up spherical coordinates (r, θ, φ) centered at the center of mass of star I. We divide the sphere into N_R concentric shells and expand the density using the associated Legendre functions $P_k^l(\cos \theta)$ as

$$\Theta^n(r_j, \theta, \varphi) = \sum_{k=0}^{\infty} \sum_{l=0}^k \rho_{kl}(r_j) P_k^l(\cos \theta) \cos l\phi, \quad (28)$$

where ρ_{kl} is the coefficients to be determined, and

$$r_j = \frac{R_L}{\alpha N_R} (j - 1/2) \quad (29)$$

denotes the radius of the j -th shell for $j = 1, 2, \dots, N_R$. Note that equation (28) does not contain $\sin l\phi$ terms because of the even symmetry about the meridional plane. Using the orthogonal properties of the Legendre functions, one can show that

$$\rho_{kl}(r_j) = \frac{2k+1}{4\pi} (2 - \delta_{l0}) \frac{(k-l)!}{(k+l)!} \int_0^\pi \int_0^{2\pi} \Theta^n(r_j, \theta, \varphi) P_k^l(\cos \theta) \cos l\varphi \sin \theta d\theta d\varphi, \quad (30)$$

where δ_{l0} is the Kronecker delta: $\delta_{l0} = 1$ for $l = 0$; $\delta_{l0} = 0$ otherwise (see e.g., Hernquist & Ostriker 1992).

For Θ^n expanded in equation (28), equation (16) yields the series solution

$$\Psi_g(r, \theta, \varphi) = - \sum_{k=0}^{\infty} \sum_{l=0}^k \left[Q_{kl}(r) r^{-k-1} + R_{kl}(r) r^k \right] P_k^l(\cos \theta) \cos l\varphi, \quad (31)$$

where

$$Q_{kl}(r) = \frac{1}{2k+1} \int_0^r r'^{k+2} \rho_{kl}(r') dr', \quad (32)$$

and

$$R_{kl}(r) = \frac{1}{2k+1} \int_r^{r_{N_R}} r'^{1-k} \rho_{kl}(r') dr', \quad (33)$$

(see e.g., Binney & Tremaine 2008). Note that equation (31) gives the gravitational potential at not only the interior but also exterior of a polytrope; Ψ_g at $r > R_L$ can be obtained by taking $Q_{kl}(r) = Q_{kl}(r_{N_R})$ and $R_{kl}(r) = R_{kl}(r_{N_R}) = 0$. As noted by Ostriker & Mark (1968), the integral representation via equations (28)-(33) of the Poisson equation (16) is favored over the differential form (eq. [16]) since the former not only incorporates the boundary conditions but also guarantees numerical convergence.

2.4. Iteration Procedure

To find the self-consistent equilibrium solution Θ for a given set of the parameters n , μ , and ν , we proceed the following steps. First, as a trial density distribution, we consider a uniform sphere with radius R_L/α and density $\Theta = 1$, consisting of $N_R = 1200$ shells. The sphere is initially rotating at $\Omega/\Omega_K = 1$. Second, we evaluate the integrals in equations (30), (32) and (33) using Gaussian and Newton-Cotes quadratures (e.g., Press et al. 1988) to obtain the coefficients $\rho_{kl}(r_j)$, Q_{ikl} , and R_{ikl} successively. The corresponding self-gravitational potential Ψ_g is then obtained from equation (31) in which the summation over the k -index is truncated after 10 terms; the associated error is negligibly small. Third, we calculate the rotation parameter ν from equation (17) and construct the effective potential Ψ . Fourth, we solve equations (13) and (20) (or, equation [19] after a temporary convergence) to update Θ and Ω/Ω_K . Fifth, we calculate the center of mass $\xi_{\text{cm}} = (\int \xi \Theta^n d^3\xi) / (\int \Theta^n d^3\xi)$ of star I using the updated Θ , and shift the coordinates so as to make ξ_{cm} coincide with the origin, while keeping star II at $\xi = (\nu, 0, 0)$ in the new coordinates. As a convergence criterion, we require the virial parameter ϵ from equation (21) to be less than 10^{-10} ; otherwise, we go back to the second step with the updated Θ and Ω/Ω_K in the shifted coordinates, and repeat the iterations until the convergence is attained. For stars with critical rotation, we find that typically 50 iterations suffice to lead to converged results.

3. Numerical Results

While the main purpose of this work is to find the changes in the internal structure of binary stars due to rotational and tidal perturbations, we first apply our method to construct equilibrium models of polytropes in isolation or in uniform rotation. This will allow us to check our SCF method as well as to quantify the effects of rotation on the stellar structure. We then explore equilibrium polytropes subject to both centrifugal and tidal forces.

3.1. Undisturbed Polytropes

We first consider undisturbed polytropes, the solutions to which can be obtained by taking $\nu = 0$, corresponding to $\Psi_\Omega = \Psi_* = 0$, in our SCF method. Table 1 lists the resulting dimensionless

parameters that we find for some selected values of n . All the values are in excellent agreement with those given in Chandrasekhar (1939), confirming the performance of our technique.

3.2. Uniformly Rotating Polytropes

If one takes $\mu = 1$ in equations (14) and (15) and regards v as a free parameter, the problem is reduced to finding solutions for polytropes under uniform rotation. Figures 2 and 3 give as solid lines the dependences upon the rotation parameter v of the mass concentration $\rho_c/\bar{\rho}$, dimensionless volume radius ξ_1 , polar radius $\xi_p = R_p/\alpha$, and equatorial radius $\xi_e = R_e/\alpha$ for rotating polytropes with $n = 3$ and 1.5, respectively. For comparison, we plot the results available from the published work, based on the first-order perturbation theory (Chandrasekhar 1933a), the second-order approximation (Anand 1968), the advanced first-order approximation (Linnell 1977, 1981), and the Legendre-polynomial expansions (James 1964) as dotted lines, dot-dashed lines, open circles, and filled circles, respectively.

As v increases from zero, the centrifugal force tends to distort the shape of a polytrope by increasing the equatorial radius at the expense of the polar radius. The polar compression is smaller than the equatorial expansion, causing the polytrope to have a larger mean radius than the non-rotating counterpart (e.g., Linnell 1981). A polytrope with faster rotation should definitely be more centrally condensed in order for self-gravity to offset the enhanced centrifugal and pressure gradient forces near the equatorial plane, as Figures 2a and 3a evidence. When v becomes sufficiently large, perturbed polytropes reach a critical state where they are on the verge of equatorial breakup. This critical rotation is formally expressed as $\partial\Phi/\partial r = 0$ at the equator, or equivalently, $\partial\Theta/\partial\xi|_{\xi=\xi_e} = 0$ when $v = v_c$, indicating that the centrifugal force barely balances the self-gravity at the equator. No equilibrium configuration exists for $v > v_c$. Table 2 gives the various parameters for the critically-distorted uniformly-rotating polytropes with differing n . The smaller n , the smaller $\rho_c/\bar{\rho}$ and the larger deviation of the gravitational potential of star I from that of a Newtonian point-mass. The values of λ_c for polytropes with indices $n = 1.0-2.5$ agree, within less than 0.2%, with the published numerical results of James (1962) (see also Hurley & Roberts 1964). Note that $\lambda_c = 0.36074$ for $n = 4.5$ polytropes are virtually the same as the value from the Roche model with $\mu = 1$ (Horedt 2004).

Although the first- and second-order perturbation methods are reasonably good for ξ_p since the centrifugal force is very small near the poles, they systematically underestimate $\rho_c/\bar{\rho}$, ξ_e , and ξ_1 as v increases toward v_c . Being valid only for $v \ll 1$, they are also unable to yield correct values of v_c . On the other hand, for the the whole range of v , our results for ξ_p and ξ_e are within 1% of the numerical values from James (1964), verifying again the accuracy of our SCF method. For practical purposes, we fit the dependences upon v/v_c of the various parameters characterizing the shapes and internal structures of rotating polytropes using a simple function

$$f(v) = a_0 + a_1\left(\frac{v}{v_c}\right) + a_2\left(\frac{v}{v_c}\right)^2 + a_3 \ln\left(1 - a_4\left[\frac{v}{v_c}\right]\right), \quad (34)$$

with coefficients a_i . Table 3 lists the fitting coefficients for $f = \xi_1, \xi_e, \xi_p, \rho_c/\bar{\rho}, N_n$, and I of rotating polytropes with $n = 1.5$ and $n = 3$; the associated fitting errors are less than 1%. Note that a_0 in each fit is identical to the corresponding value of non-rotating polytropes.

It is interesting to compare the shapes of rotationally-distorted polytropes with those under the Roche approximation that assumes that the stellar gravity is dominated by the central mass concentration and that the polar radius is unchanged due to rotation. The main predictions of the Roche models are that the ratio of the equatorial velocity V_e to the critical value V_c behaves with the aspect ratio $\mathcal{R} \equiv \xi_e/\xi_p$ as

$$\frac{V_e}{V_c} = \sqrt{\frac{3(\mathcal{R} - 1)}{\mathcal{R}}}, \quad (35)$$

and that $\mathcal{R}_c = 1.5$ in the case of critical rotation (e.g., Collins 1963; Baumgarte & Shapiro 1999; Townsend et al. 2004). Figure 4a plots as a solid line the change in \mathcal{R}_c of rotating polytropes with varying n , while Figure 4b gives V_e/V_c as a function of \mathcal{R} for various polytropic and the Roche models. In terms of \mathcal{R}_c , the Roche models are a good approximation for polytropes with very high mass concentration toward their centers (relative errors less than 3% for $n \gtrsim 2.0$). On the other hand, equation (35) is quite accurate for polytropes with $n = 1.5$ except near the critical configuration. It underestimates V_e/V_c for polytropes with $n \gtrsim 3.0$ by about 10%, while overestimating for $n = 0.5$ polytropes by about 15%. This suggests that one should be cautious when estimating the equatorial velocity from an observed aspect ratio of a rapidly rotating star.

3.3. Rotationally and Tidally Distorted Polytropes

When a binary star with a given polytropic index n is subject to both tidal and centrifugal distortions, its internal structure is determined solely by the two parameters in our formulation: its relative mass μ and the dimensionless orbital separation ν ; for systems in synchronous rotation, the rotation parameter v is given automatically via equations (17) and (19). Figure 5 plots the dependences of v upon ν for the equilibrium polytropes under both tidal and centrifugal forces. Each solid line corresponds to a sequence of equilibrium models with a fixed relative mass μ displayed in the panels. Note that v monotonically decreases with increasing orbital separation along each sequence, becoming vanishingly small at $\nu \rightarrow \infty$. On the other hand, a polytrope becomes distorted more and more as ν decreases along a given sequence. When ν becomes sufficiently small, it eventually reaches a critical state beyond which self-gravity no longer balances the combined tidal and centrifugal forces at the equator. The filled circles marked at the uppermost tips of the sequences correspond to the critical points (ν_c, v_c) . In what follows, we use the term “critical component” to refer to star I in critical configuration. The dotted line connecting the critical points draws the locus of the critical components in the ν - v plane, above which no equilibrium polytrope exists.

3.3.1. Shape, Size, and Internal Structure

Figure 6*a-c* illustrates how the shapes on the meridional plane of $n = 3$ equilibrium polytropes change as the amplitude of tidal and rotational perturbations varies. All the models have $\mu = 0.5$. The corresponding Roche lobe around star I is plotted as a dotted line. In each panel, the inner solid contours draw equidensity surfaces with $\rho/\bar{\rho} = 3^{-m}(\rho_c/\bar{\rho})_{\text{iso}}$, where $m = 0, 1, \dots, 5$ from inside to outside, while the outermost contour represents the boundary of a perturbed polytrope. Here and in what follows, the subscript “iso” indicates the quantities of the corresponding isolated polytrope. When ν is sufficiently large, the tidal and rotational perturbations are so weak that a polytrope is in an almost spherical configuration, with the central density only slightly larger than the unperturbed value (Fig. 6*a*). As ν decreases, the enhanced perturbations make the polytrope larger and more centrally concentrated (Fig. 6*b*). It is remarkable that when $\nu = \nu_c$ ($= 18.81$ for $n = 3$), the outer envelope of the critical component fills the Roche lobe almost completely, while the dense inner-part still remains nearly spherical (Fig. 6*c*).

Figure 6*d* plots the outer boundaries of the critical components with differing n for $\mu = 0.5$. When $n \gtrsim 2$, a critical component has a boundary virtually identical to its Roche lobe. With relatively low central concentrations, polytropes with $n \lesssim 1$ become flattened toward the equatorial plane, although the deviation from the Roche lobe is still slight. Figure 7 gives a quantitative comparison between the volume radius R_1 of a critical component and the effective radius R_L of the Roche lobe fitted by Eggleton (1983)

$$\frac{R_L}{A} = \frac{0.49q^{2/3}}{0.6q^{2/3} + \ln(1 + q^{1/3})}, \quad (36)$$

where $q \equiv M_1/M_2 = \mu/(1 - \mu)$. Indeed, Eggleton’s formula is an excellent approximation to R_1 , with a relative error less than 2%, for polytropes with $n \gtrsim 2$. For small values of n , R_L overestimates R_1 because of the equatorial flattening. For $n = 3/2$ polytropes, we find

$$\frac{R_1}{A} = \frac{0.5126q^{0.7388}}{0.6710q^{0.7349} + \ln(1 + q^{0.3983})}, \quad \text{for } n = 3/2, \quad (37)$$

gives a good fit (within $\sim 1 - 2\%$ for $10^{-2} < q < 10^4$) to the volume radius.

Figures 8 and 9 plot the variations of $\rho_c/\bar{\rho}$, ξ_1 , N_n , and I of rotationally- and tidally-distorted polytropes with $n = 1.5$ and 3.0 against the relative radius $R_A \equiv \xi_1/\nu = R_1/A$ as solid lines. Again, the dotted line connecting the top ends of the constant- μ sequences in each panel corresponds to the critical components. As expected, the central density concentration, volume radius, and moment of inertia increase as the perturbation amplitude increases. The relative increment of $\rho_c/\bar{\rho}$ is greater for polytropes with larger n . Note that the largest changes in these quantities occur when $\mu = 1$, corresponding to purely rotating polytropes; in synchronized binaries with $0.1 \lesssim \mu \lesssim 0.9$, the variations of $\rho_c/\bar{\rho}$, ξ_1 , and N_n are less than 10% even in critical configurations. The dependences of these quantities on R_A for a fixed value of μ can be approximated by

$$g(R_A) = b_0 + b_1 R_A + b_2 R_A^2 + b_3 R_A^3 \exp(b_4 R_A), \quad (38)$$

with $g = \rho_c/\bar{\rho}$, ξ_1 , N_n , or I . The fitting coefficients b_i are given in Tables 4, 5, 6, and 7, respectively; the fits are accurate within 1%. Note that b_0 's in each Table are identical to the values for the unperturbed polytropes.

Since α depends on ρ_c which in turn varies with ν and μ , the dimensionless volume radius ξ_1 shown in Figure 8 does not give direct information on the change of a stellar size due to centrifugal and tidal forces. Assuming that the perturbations do not modify the pressure constant K (equivalently, specific entropy or degeneracy; see e.g., Burrows & Liebert 1993) inside a star, equation (23) gives $R_1/R_{1,\text{iso}} = (N_n/N_{n,\text{iso}})^{n/(n-3)}$ as the size ratio of distorted to unperturbed polytropes with the same mass. Figure 10 plots $R_1/R_{1,\text{iso}}$ as solid lines for polytrope with $n = 1.5$ and 3.5 , showing that stars become bigger as the amplitude of perturbations increases.¹ For $n = 3.5$ polytropes in critical configuration, the enhancement factor in the stellar size is $\sim 12\%$ for $\mu = 1$ and $\sim 2 - 3\%$ for $\mu \sim 0.1 - 0.9$, while it increases to $\sim 23\%$ for $\mu = 1$ and $\sim 4 - 8\%$ for $\mu \sim 0.1 - 0.9$ for $n = 1.5$ polytropes. Taken together with the results for $\rho_c/\bar{\rho}$ discussed above, this implies that polytropes with smaller n adjust themselves to the perturbations by increasing their size more than being centrally condensed, while those with larger n do so by increasing the density concentration more.

In the dynamical study of close binary systems such as mass transfer, the spin angular momentum is often neglected compared to the orbital angular momentum. To check if this is a reasonable assumption, we plot in Figure 11 the dependences of $J_{\text{spin}}/J_{\text{orb}}$ on ξ_1/ν and μ as solid lines. Overall, $J_{\text{spin}}/J_{\text{orb}}$ is well approximated by

$$\frac{J_{\text{spin}}}{J_{\text{orb}}} = \frac{c_0}{(1 - \mu)^2} \left(\frac{\xi_1}{\nu} \right)^2, \quad (39)$$

with the coefficient $c_0 = 0.20460$ and 0.07536 for $n = 1.5$ and 3 cases, respectively.² The fit is almost exact for small ξ_1/ν , and the maximum error occurring at the critical values of ξ_1/ν is less than 5%. Apparently, the contribution of the spin angular momentum to the total is negligible for wide binaries where $\xi_1/\nu \ll 1$. Notice, however, that when a binary star with sufficiently large μ is near the critical configuration, J_{spin} even exceed J_{orb} and can thus be dynamically important.

For the critical components, $\rho_c/\bar{\rho}$, N_n , $J_{\text{spin}}/J_{\text{orb}}$, and I can be approximated within 1% of accuracy by

$$\rho_c/\bar{\rho} = 5.9907 + \frac{0.2755q^{0.8849}}{0.2430q^{0.8258} + \ln(1 + q^{1.1415})}, \quad \text{for } n = 1.5, \quad (40a)$$

$$\rho_c/\bar{\rho} = 54.1825 + \frac{5.3141q^{0.9486}}{0.2712q^{0.8933} + \ln(1 + q^{1.1494})}, \quad \text{for } n = 3, \quad (40b)$$

¹As is well known, it is not viable to constrain the radius from the mass for polytropes with $n = 3$ (e.g., Chandrasekhar 1939).

²In the limit of $\xi_1/\nu \rightarrow 0$, it can be shown that $c_0 = 3I(\rho_c/\bar{\rho})(4\pi\xi_1^5)^{-1}$ for unperturbed polytropes.

$$N_n = 0.42422 - \frac{0.0191q^{0.9561}}{0.3557q^{0.9130} + \ln(1 + q^{1.1635})}, \quad \text{for } n = 1.5, \quad (41a)$$

$$N_n = 0.36394 - \frac{0.00207q^{1.01714}}{0.35430q^{1.00296} + \ln(1 + \mu^{1.08931})}, \quad \text{for } n = 3, \quad (41b)$$

$$\frac{J_{\text{spin}}}{J_{\text{orb}}} = \begin{cases} 0.076q^{1.858} + 0.043q^{0.645}, & \text{if } q < 0.5, \\ 0.068(q - 0.5)^{2.106} + 0.100q^{0.9}, & \text{if } q \geq 0.5, \end{cases} \quad \text{for } n = 1.5, \quad (42a)$$

$$\frac{J_{\text{spin}}}{J_{\text{orb}}} = \begin{cases} 0.026q^{1.853} + 0.015q^{0.651}, & \text{if } q < 0.5, \\ 0.026(q - 0.5)^{2.061} + 0.037q^{0.9}, & \text{if } q \geq 0.5, \end{cases} \quad \text{for } n = 3, \quad (42b)$$

and

$$I = 93.1560 + \frac{15.5476q^{0.9334}}{0.3795q^{0.8902} + \ln(1 + q^{1.1985})}, \quad \text{for } n = 1.5, \quad (43a)$$

$$I = 90.910 + \frac{4.4373q^{0.9879}}{0.5200q^{0.9560} + \ln(1 + q^{1.1593})}, \quad \text{for } n = 3, \quad (43b)$$

for the range of $0.05 < q < 40$.

3.3.2. Rotational vs. Tidal Distortion

Figure 12 plots as solid curves v_c and ν_c for the critical components with $n = 1.5$ and 3.0 as functions of μ . These are fitted to

$$v_c \cdot 10^3 = 4.08028 + 4.10(1 - \mu) - 0.54(1 - \mu)^2 - 6.58(1 - \mu)^{0.46} \quad \text{for } n = 1.5, \quad (44a)$$

$$v_c \cdot 10^2 = 4.35828 + 4.55(1 - \mu) - 0.79(1 - \mu)^2 - 7.15(1 - \mu)^{0.43} \quad \text{for } n = 3, \quad (44b)$$

and

$$\nu_c = \begin{cases} \sum_{i=0}^5 d_i(1 - \mu)^i & \text{if } 0.1 < \mu < 1, \\ e_0 + e_1\mu^{-1/3} & \text{if } \mu < 0.1, \end{cases} \quad (45)$$

with the coefficients d_i and e_i given in Table 8. Filled circles in Figure 12a represent the results of Singh & Singh (1983) under the double approximation, which are within $\sim 10\%$ of our fully self-consistent values. While Singh & Singh (1983) found that v_c monotonically increases with μ ($\gtrsim 0.09$), our results show that v_c attains a minimum at $\mu_{\text{min}} \sim 0.13 - 0.14$ for $n \gtrsim 1.5$.

For $\mu > \mu_{\text{min}}$, the rotational effect is more important than the tidal force in maintaining equilibria of critical components (e.g., Russell 1928).³ As μ increases, star I would feel a weaker

³Russell (1928) considered the ratio of the tidal to centrifugal forces at the *undistorted* stellar surface, and found that tidal and rotational effects are the same when $\mu = 1/6$, which is not much different from μ_{min} that we have found.

tidal force from its companion if the orbital distance were the same. Therefore, star I must rotate faster to be critical, increasing v_c . This in turn corresponds to decreasing ν_c due to the condition of spin-orbit synchronization. In the limit of $\mu \rightarrow 1$, v_c converges to the value found in §3.2 for critical rotation in the absence of the tidal force, while ν_c is tending to ξ_e , suggesting that a fictitious secondary with vanishing mass is located at the equator of the primary in critical condition.

When $\mu < \mu_{\min}$, on the other hand, the tidal force dominates the centrifugal force in the force balance. Note that v is proportional to the ratio of the tidal force to the self-gravity at $r \approx R_1$, so that $v_c \propto (\xi_1/\nu_c)^3/\mu$. Eggleton’s formula (eg. [36]) shows that ξ_1/ν_c decreases slightly more slowly than $\mu^{1/3}$ as μ decreases. This causes v_c to increase slowly as μ decreases from μ_{\min} . In the limit of $\mu \rightarrow 0$, $\nu_c \propto \mu^{-1/3}$, and v_c converges to 1.1530×10^{-2} and 1.2496×10^{-3} for the cases with $n = 1.5$ and 3.0 , respectively.⁴ Figure 13 plots the variation of μ_{\min} with the polytropic index, which shows that $\mu_{\min} = 0.136$ as n approaches 5.⁵ For lower values of n , the enhanced equatorial radii due to flattening (e.g., Fig. 6d) make the centrifugal force more important at the surface, tending to decrease μ_{\min} .

3.3.3. Structure Constant k_2

Once the three-dimensional density distributions of disturbed polytropes are found, it is straightforward to calculate the apsidal motion constant k_2 defined by

$$k_2 = \frac{3 - \eta_2(\xi_1)}{4 + 2\eta_2(\xi_1)}, \quad (46)$$

where $\eta_2(\xi_1)$ is the solution at the volume radius of the Radau equation that describes the distortion of equidensity surfaces inside a perturbed polytrope (see, e.g., Kopal 1978). For isolated polytropes, we have confirmed that equation (46) yields $\log k_{2,\text{iso}} = -0.8438$, -1.8403 , and -2.3081 for $n = 1.5$, 3.0 , and 3.5 cases, respectively, which are in good agreement with the published results (e.g., Brooker & Olle 1955).

Figure 14 plots as solid lines the changes of $\Delta \log k_2 \equiv \log(k_2/k_{2,\text{iso}})$ with respect to the rotation parameter λ and the central density concentration $\Delta \log \rho_c/\bar{\rho} \equiv \log[(\rho_c/\bar{\rho})/(\rho_c/\bar{\rho})_{\text{iso}}]$ for distorted polytropes with $n = 1.5$, 3.0 , and 3.5 . Clearly, k_2 decreases as the perturbation amplitude (or, the degree of central concentration) increases. Using realistic ZAMS models with modern opacities for unperturbed stars, but by relying on a quasi-spherical or double-approximation method in

⁴For the Roche model, Horedt (2004) showed that the mean critical rotation parameter is $\lambda_c \approx 2^4/3^5$ for a vanishingly small μ (see also Kopal 1989). This corresponds to $v_c = \lambda_c/(\rho_c/\bar{\rho}) \approx 1.002 \times 10^{-2}$ and 1.041×10^{-3} , since $\rho_c/\bar{\rho} = 6.5721$ and 63.2685 when $\mu \rightarrow 0$ for $n = 1.5$ and 3.0 , respectively. These are in reasonable agreement with our results for the critical components.

⁵Using the Roche model, Kopal (1978) found the minimum value of λ_c occurs in between $\mu = 0.130$ and 0.167 (or $q = 0.15$ and 2), which is consistent with our results.

evaluating the sole effect of stellar rotation, Stothers (1974) and Claret (1999) found $\Delta \log k_2 = -0.7\lambda$ and $\Delta \log k_2 = -0.87\lambda$, respectively. These are plotted as dotted and dashed lines in the left panels of Figure 14, approximately enveloping our results for $n = 3.5$. While it is not straightforward to compare our results with those of Stothers (1974) and Claret (1999) since the unperturbed stellar models are different, this suggests that rotationally-distorted stellar models considered by these authors likely have internal structures similar to those of $n = 3.5$ polytropes. The right panels of Figure 14 show that for polytropes with fixed n , $\Delta \log k_2$ varies approximately linearly with $\Delta \log \rho_c/\bar{\rho}$, nearly independent of μ , with an average slope of -1.12 , -1.33 , and -1.39 for $n = 1.5$, 3.0 , and 3.5 cases, respectively. This confirms the notion that k_2 is inversely proportional to the central density concentration (Stothers 1974). Figure 14 also shows that $|\Delta \log k_2| < 0.1$ for $\mu \lesssim 0.9$, while it can be as large as 0.3 for strongly centrally-condensed polytropes in critical rotation with $\mu = 1$. This suggests that the decrease in k_2 due to both rotational and tidal distortions is much smaller in binary stars with synchronous rotation than in purely rotating stars.

4. Apsidal Motion

Stars in close binaries have a shape that deviates from a spherical configuration, rendering the orbits of their companions non-Keplerian. As mentioned in the Introduction, it is well known that tidal and rotational distortions cause the apsidal line to advance, the rate of which depends on the degree of stellar concentration. Many observational studies have employed the analytic formulae of Cowling (1938) and Stern (1939), which are an eccentric extension of Russell (1928) formula applicable to near-circular orbits. By retaining only the linear-order terms, however, all of these formulae are valid in a strict sense when the tidal and rotational distortions are very small. Even in the cases when the effects of dynamical tides and relativity are unimportant, however, the distortion of a stellar shape can be substantial especially for critical components. In this section, we check the validity of the classical formula of Russell (1928) using self-consistent solutions for stars in circular-orbit binaries for which tides are stationary.

To obtain the apsidal motion rates from our distorted polytropes, we calculate the self-gravitational potential Φ_g numerically along the axis joining the two binary components after the self-consistent solutions are obtained. We then apply the orbit theory in which the rate of change of the periastron is given by

$$\dot{\varpi} = \Omega - \kappa, \quad (47)$$

where

$$\kappa \equiv \frac{M}{M_1 A^3} \left. \frac{\partial(x^3 \Phi_g)}{\partial x} \right|_{\mathbf{x}=(A,0,0)} \quad (48)$$

is the epicycle frequency at the location of star II (e.g., Murray & Dermott 1999). The resulting (numerical) apsidal motion rates, $\dot{\varpi}_n$, versus the relative radius $R_1/A = \xi_1/\nu$ are shown as solid lines in Figure 15 for $\mu = 0.1, 1.0$ and $n = 1.5, 3.0, 3.5$ cases. Also plotted as dotted lines are

the (theoretical) rates, $\dot{\varpi}_t$, from the classical formula (eq. [1]) with k_2 calculated in §3.3.3. When the relative radius is small (i.e., $\xi_1/\nu < 0.15$ for $\mu = 0.1$ and $\xi_1/\nu < 0.5$ for $\mu = 1$) and thus the rotational and tidal perturbations are weak, the agreement between $\dot{\varpi}_n$ and $\dot{\varpi}_t$ are remarkably good. As the amplitude of perturbations increases further, however, the classical formula begins to underestimate the real apsidal motion rates. This is because the the distortion of star I becomes no longer in the linear regime as ξ_1/ν approaches the critical values. In addition, we found that the gravitational potential due to a highly distorted component has a non-negligible contribution from terms proportional to x^{-2} , while the classical theory took only x^{-3} or higher-order terms (see, e.g., Stern 1939), making $\dot{\varpi}_t$ smaller than $\dot{\varpi}_n$.

Figure 16 plots the relative difference $(\dot{\varpi}_n - \dot{\varpi}_t)/\dot{\varpi}_t$ of the numerical and theoretical rates of the apsidal motions for critical configurations as a function of μ . For critically distorted polytropes with $n = 1.5$, the real apsidal motion rates are larger by $\sim 50\%$ than the values predicted by the classical theory. As n increases, the fractional mass occupying outer layers that exhibit large distortions decreases, yielding $(\dot{\varpi}_n - \dot{\varpi}_t)/\dot{\varpi}_t \sim 5 - 15\%$ for stars with $n = 3.5$. These results suggest that the classical formula still works quite well for stars with large density concentration at centers, while it underestimates the apsidal motion rates significantly for stars with relatively low $\rho_c/\bar{\rho}$, such as in low-mass convective stars.

Finally, we define the “effective” internal structure constant $k_{2,\text{eff}}$ through

$$\frac{\dot{\varpi}_n}{\Omega_K} = k_{2,\text{eff}} \left(\frac{\xi_1}{\nu} \right)^5 \left(1 + 7 \frac{1 - \mu}{\mu} \right). \quad (49)$$

We note that $k_{2,\text{eff}}$ introduced in equation (49) is simply to match the real apsidal motion rates by means of the classical theory with the modified values of k_2 , and thus it should not be interpreted as conveying physical information on the internal structure of perturbed stars. Figure 17 shows the dependence of $\Delta \log k_{2,\text{eff}} \equiv \log(k_{2,\text{eff}}/k_{2,\text{iso}})$ on λ for $n = 1.5$ and 3.5 polytropes. Dotted lines correspond to the cases with critically distorted polytropes. Note that $\Delta \log k_{2,\text{eff}}$ even increases with increasing λ when n is small, although this does not mean stars become less centrally-condensed as the amplitude of perturbations increases. For practical uses, we fit $k_{2,\text{eff}}$ using

$$\Delta \log k_{2,\text{eff}} = a_1 \lambda + a_2 \lambda^2 + a_3 \lambda^3, \quad (50)$$

with the coefficients a_i listed in Table 9 for $n = 1.5, 3.0,$ and 3.5 cases. The relative errors of the fits are less than 2%.

5. Summary and Discussion

Binary stars are a traditional source of information on stellar mass, radius, luminosity, etc., the inter-relationships of which are of crucial importance to stellar astrophysics. Many observational and theoretical arguments suggest that centrifugal and tidal forces may significantly affect the

physical properties of stars in close binary systems. Since the pioneering work of Chandrasekhar (1933a,b,c), there have been numerous theoretical studies that tried to find equilibrium solutions of polytropic stars under rotational and tidal perturbations. However, most of them take some type of approximations, and thus are valid only when the perturbations are weak. In order to construct equilibrium structures of such polytropes without relying on any assumption on the perturbation strength and the degree of stellar distortion, we use an SCF method in which the angular orbital velocity Ω is self-consistently constrained rather than being treated as a free parameter.

To ignore the complicated effects of time-dependent tides and to make contact with the previous theoretical work, we consider a circular-orbit, synchronized binary consisting of a polytrope and a point-mass object. Based on our SCF scheme described in §2, we solve the dimensionless steady-state momentum equation (13) and Poisson equation (16) in the rotating frame at Ω , alternately and iteratively, until the converged solutions are obtained. We first apply our method to polytropes in isolation and subsequently in uniform rotation, and calculate the density concentration $\rho_c/\bar{\rho}$, the volumn radius ξ_1 , the equatorial radius ξ_e , and the polar radius ξ_p ; these are in good agreement with the accurate results of Chandrasekhar (1939) for unperturbed polytropes and James (1964) for rotating polytropes, confirming the performance of our SCF method. When the rotation parameter v (eq. [17]) is sufficiently large, a rotating polytrope reaches a critical state, beyond which no equilibrium is possible. Equation (34) and Table 3 provide fitting formulae of ξ_1 , ξ_e , ξ_p , $\rho_c/\bar{\rho}$, N_n , and the moment of inertia I for polytropes with $n = 1.5$ or 3 . By comparing the axis ratio $\mathcal{R} = \xi_e/\xi_p$ and the velocity ratio V_e/V_c with the predictions from the conventional Roche model, we find that in terms of the critical value \mathcal{R}_c , the Roche model is a reasonable approximation for rapidly rotating stars with high central density concentration (i.e., when $n \gtrsim 2.0$), although it underestimates V_e/V_c by about 10% when $n \gtrsim 3.0$.

We then calculate equilibrium solutions of polytropes subject to both centrifugal and tidal forces. The rotational and tidal perturbations in general make disturbed stars larger in size and more condensed toward their centers. For $n = 1.5$ polytropes in critical configurations, for example, the distorted stars are larger by $\sim 23\%$ and $\sim 4-8\%$ for $\mu = 1$ and $\mu \sim 0.1-0.9$, respectively, than the unperturbed counterparts with the same specific entropy. Here, μ is the mass of a perturbed star relative to the total mass of a binary system. For more centrally-concentrated polytropes with $n = 3.5$, the enlargement factor is reduced to $\sim 12\%$ and $\sim 2-3\%$ for $\mu = 1$ and $\mu \sim 0.1-0.9$, respectively. In determining the structure of a critical component, the rotational effect is more important than the tidal effect provided $\mu > \mu_{\min} \sim 0.13-0.14$. As in purely rotationally-distorted cases, the shape and size of both rotationally- and tidally-perturbed polytropes are well described by the Roche models as long as $n \gtrsim 2$. Equation (38) and Tables 4, 5, 6, and 7 give functional fits of $\rho_c/\bar{\rho}$, ξ_1 , N_n , and I on the mass ratio μ and the relative radius $R_1/A = \xi_1/\nu$, while equation (39) is for the fit of $J_{\text{spin}}/J_{\text{orb}}$, the ratio of spin to orbital angular momenta of star I. Equations (40)-(45) and Table (8) give the dependences on μ of $\rho_c/\bar{\rho}$, N_n , $J_{\text{spin}}/J_{\text{orb}}$, I , v_c , and ν_c for critical configurations.

Using self-consistent equilibrium solutions of rotationally- and tidally-distorted polytropes,

we calculate the internal structure constant k_2 by integrating the Radau equation as well as the apsidal motion rate $\dot{\varpi}_n$ based on the orbit theory. We find that $\Delta \log k_2$ depends almost linearly upon $\Delta \log \rho_c/\bar{\rho}$, with an average slope of -1.12 , -1.33 , and -1.39 , nearly independent of μ , for $n = 1.5$, 3.0 , and 3.5 polytropes, respectively. The expression $\Delta \log k_2 \sim -(0.7 - 0.87)\lambda$ found for rotating stars from Stothers (1974) and Claret (1999) appears to be valid only for stars with very high density concentration, corresponding to $n \approx 3.5$. The comparison of $\dot{\varpi}_n$ calculated from our SCF method with $\dot{\varpi}_t$ from the classical formula of Russell (1928) based on the first-order perturbation analyses shows that the latter is valid only when the amplitude of perturbations is small. For the cases of critical configurations where tidal and centrifugal forces are rather strong, the classical theory underestimates the real apsidal motions rates by as much as $\sim 50\%$ for $n = 1.5$ polytropes and $\sim 5 - 15\%$ for $n = 3.5$, indicating that the nonlinear effects are by no means negligible in augmenting the apsidal motion rates. To this end, we define the effective internal structure constant $k_{2,\text{eff}}$ that gives the real apsidal motion rates by means of the classical formula. Equation (50) and Table 9 present the algebraic fits to $k_{2,\text{eff}}$.

Observations of eclipsing binary stars indicate that B-type binary stars are about 20% smaller in size than the single stars of the same spectral type, while A- and F-type binary stars are larger than the corresponding isolated stars (e.g., Malkov 2003, 2007). For M-type stars with mass $0.4 - 0.8 M_\odot$, Ribas (2006) reported that observed radii of eclipsing binary stars are larger by $5 - 10\%$ than those of the theoretical, isolated models. On the other hand, our self-consistent calculations show that centrifugal and tidal perturbations make binary stars bigger in size. These observational and theoretical results are qualitatively reconciled with each other if one considers the fact that early-type (late-type) binary stars rotate slower (faster) than the isolated counterparts (e.g., McNally 1965; Malkov 1993, 2003). Slow rotations of early-type stars in close binaries are apparently a consequence of the spin-orbit synchronization occurring during their main-sequence phase, induced by tidal torque due to either radiative damping of dynamical tides (Zahn 1977) or large-scale mechanical currents (Tassoul 1987, 1988). In addition, early-type binary stars appear to have a low initial rotational velocity amounting to $\sim 130 \text{ km s}^{-1}$, compared to $\sim 200 \text{ km s}^{-1}$ for single stars, when they enter the ZAMS stage (Khaliullin & Khaliullina 2007).

By analyzing the near-IR, long-baseline interferometric data of the Be star Achernar which is known as a rapid rotator, Domiciano de Souza et al. (2003) reported that the star has a projected aspect ratio of $\mathcal{R} = 1.56 \pm 0.05$. Since the projection always tends to decrease the measured aspect ratio, this implied that the real oblateness must be larger than the critical value under the Roche approximation. If Achernar can be modeled by a single, rigidly-rotating polytrope, Figure 4a suggests that it must have $n < 2.0$, which is unlikely given that Be stars may have a larger central density concentration than that of a polytrope with $n = 3$. Jackson et al. (2004) showed that differentially-rotating stellar models with a more realistic equation of state allow equilibrium stars with \mathcal{R} larger than 1.5, compatible with the interferometric observations. On the other hand, Carciofi et al. (2008) found that the data are also consistent with a critically-rotating central star surrounded by a small equatorial disk produced by the ejected material from the central star.

If one component (star I) in a semidetached binary overfills its Roche lobe, it may rapidly lose mass to its companion in a few orbital periods. Such dynamical mass transfer is likely to create a common envelope binary, important for the evolution of cataclysmic binaries and double degenerate white dwarfs (e.g., Paczyński 1976; Frank et al. 2002). In finding the condition for the onset of the dynamical mass transfer, most previous work considered the conservation of the orbital angular momentum, neglecting the contribution of the spin angular momentum. Using the Eggleton formula (eq. [36]) for the Roche lobe radius, for instance, Hjellming & Webbink (1987) found that the rapid conservative mass transfer from an $n = 1.5$ polytrope to its compact companion occurs if $q = M_1/M_2 > q_c = 0.634$, while the use of the less accurate Paczyński (1971) formula, $R_L/A = 0.4622(q/[1+q])^{1/3}$, yields $q_c = 2/3$ (Rappaport et al. 1982; D’Souza et al. 2006; Motl et al. 2007). We revisit this issue using the conservation of the total angular momentum that includes J_{spin} given by equation (39), and find that the critical value of q for the dynamical mass transfer is increased to $q_c = 0.693$ and 0.736 under the Eggleton and Paczyński formulae, respectively, for $n = 1.5$ polytropes. Note that the value of q_c based on the Eggleton formula including J_{spin} is similar to that under the Paczyński formula without the effect of J_{spin} . Although the changes in q_c due to the inclusion of the spin angular momentum are not great since $J_{\text{spin}}/J_{\text{orb}} \lesssim 0.1$ for $q < 1$ (or $\mu < 0.5$), the effect of J_{spin} can be significant in the processes of mass transfer if the donor-to-accretor mass ratio is large.

Measuring apsidal motion rates is probably a unique means to probe the internal density concentration of binary stars. For systems where the effects of general relativity (Giménez 1985) or a third body (e.g., Bozkurt & Değirmenci 2007) are unimportant, most previous studies adopted the classical theory of Stern (1939) with k_2 calculated from isolated polytropes and found that binary stars are much more centrally condensed than predicted (e.g., Schwarzschild 1958; Kopal 1978). More recently, Claret & Giménez (1993) and Claret & Willems (2003) showed the theoretical results are in good agreement with observations if the changes of k_2 due to rotation as well as the effects of the initial chemical composition and convective core overshooting are taken into account. However, the reduction of k_2 considered in these papers amounts to $\Delta \log k_2 \sim -(0.2 - 0.3)$, which may be possible only for purely rotating cases with $\mu = 1$. Even for highly centrally-concentrated polytropes with $n = 3.5$, Figure 14 shows that $|\Delta \log k_2| < 0.1$ for synchronous binaries in the mass range of $0.1 \lesssim \mu \lesssim 0.9$. In addition, our SCF analyses show that the classical formula derived under the linear approximation is likely to underestimate the real apsidal motion rates for stars with low central concentration, especially in critical configurations. All of these suggest that special care should be taken in interpreting observed data for apsidal motions of close binary systems where stellar rotation is slow.

The authors acknowledge a helpful report from an anonymous referee, and Jeremiah P. Ostriker for a careful reading of the manuscript. This work was supported by the Creative Research Initiatives program, CEOU of MEST/KOSEF.

REFERENCES

- Anand, S. P. S. 1968, *ApJ*, 153, 135
- Arbutina, B. 2009, *MNRAS*, 394, 501
- Baumgarte, T. W., & Shapiro, S. L. 1999, *ApJ*, 526, 937
- Binney, J., & Tremaine, S. 2008, *Galactic Dynamics*, 2nd ed. (Princeton: Princeton Univ. Press), 81
- Bozkurt, Z., & Değirmenci, Ö. L. 2007, *MNRAS*, 379, 370
- Brooker, R. A., & Olle, T. W. 1955, *MNRAS*, 115, 101
- Burrows, A., & Liebert, J. 1993, *Rev. of Mod. Phy.*, 65, 301
- Carciofi, A. C., Domiciano de Souza, A., Magalhães, A. M., Bjorkman, J. E., & Vakili, F. 2008, *ApJ*, 676, L41
- Chandrasekhar, S. 1933, *MNRAS*, 93, 390
- Chandrasekhar, S. 1933, *MNRAS*, 93, 449
- Chandrasekhar, S. 1933, *MNRAS*, 93, 462
- Chandrasekhar, S. 1939, *An introduction to the study of stellar structure* (Chicago Univ. Press)
- Claret, A. 1999, *A&A*, 350, 56
- Claret, A., & Giménez, A. 1993, *A&A*, 227, 487
- Claret, A., & Willems, B. 2003, *A&A*, 410, 289
- Clement, M. J. 1974, *ApJ*, 194, 709
- Cowling, T. G. 1938, *MNRAS*, 98, 734
- Collins, G. W. 1963, *ApJ*, 128, 1134
- Domiciano de Souza, A., Kervella, P., Jankov, S., Abe, L., Vakili, F., di Folco, E., & Paresce, F. 2003, *A&A*, 407, L47
- D’Souza, M. C. R., Motl, P. M., Tohline, E., & Frank, J. 2006, *ApJ*, 643, 381
- Durney, B. R., & Roxburgh, I. W. 1970, *MNRAS*, 148, 239
- Eggleton, P. P. 1983, *ApJ*, 268, 368

- Eggleton, P. P. 2006, *Evolutionary Processes in Binary and Multiple Stars* (Cambridge: Cambridge Univ. Press)
- Frank, J., King, A. R., & Raine, D. J. 2002, *Accretion Power in Astrophysics*, 3rd ed. (Cambridge: Cambridge Univ. Press)
- Geroyannis, V. S., Tokis, J. N., & Valvi, F. N. 1979, *Ap&SS*, 64, 359
- Geroyannis, V. S., & Valvi, F. N. 1985, *ApJ*, 299, 695
- Geroyannis, V. S. 1988, *ApJ*, 327, 273
- Giménez, A. 1985, *ApJ*, 297, 405
- Giménez, A. 2007, in *IAU Symp. 240: Binary Stars as Critical Tools & Tests in Contemporary Astrophysics*, eds. W.I. Hartkopf, E.F. Guinan, & P. Harmanec (Cambridge: Cambridge Univ. Press), 290
- Gnedin, O. Y. 2003, *ApJ*, 589, 752
- Hachisu, I. 1986a, *ApJS*, 61, 479
- Hachisu, I. 1986b, *ApJS*, 62, 461
- Hachisu, I., Eriguchi, Y., & Nomoto, K. 1986a, *ApJ*, 308, 161
- Hachisu, I., Eriguchi, Y., & Nomoto, K. 1986b, *ApJ*, 311, 214
- Hernquist, L., & Ostriker, J. P. 1992, *ApJ*, 386, 375
- Hernquist, L., Sigurdsson, S., & Bryan, G. L. 1995, *ApJ*, 446, 717
- Hjellming, M. S., & Webbink, R. F. 1987, *ApJ*, 318, 794
- Horedt, G. P. 2004, *Polytropes : Applications in Astrophysics and Related Fields*, *Astrophysics and Space Science Library Vol. 306* (Kluwer Academic Publishers: Dordrecht), 198
- Hurley, M., & Roberts, P. H. 1964, *ApJ*, 180, 583
- Jackson, S. 1970, *ApJ*, 160, 685
- Jackson, S., MacGregor, K. B., & Skumanich, A. 2004, *ApJ*, 606, 1196
- Jackson, S., MacGregor, K. B., & Skumanich, A. 2005, *ApJS*, 156, 245
- James, I. 1962, Ph.D. Thesis, Manchester University
- James, R. A. 1964, *ApJ*, 140, 552
- Khaliullin, Kh. F., & Khaliullina, A. I. 2007, *MNRAS*, 382, 356

- Kopal, Z. 1972, *Adv. Astron. Ap.* 9, 1
- Kopal, Z. 1978, *Dynamics of Close Binary Systems* (Reidel: Dordrecht)
- Kopal, Z. 1989, *The Roche Problem* (Kluwer Academic Publishers: Netherlands)
- Kippenhahn, R., & Thomas, H-C. 1970, *Stellar Rotation*, ed. A. Slettebak, I.A.U. Coll. 4, (Reidel: Dordrecht)
- Lal, A. K., Saini, S., Mohan, C., & Singh, V. P. 2006, *Ap&SS*, 306, 165
- Linnell, A. P. 1977, *Ap&SS*, 48, 165
- Linnell, A. P. 1981, *Ap&SS*, 80, 501
- MacGregor, K. B., Jackson, S., Skumanich, A., & Metcalfe, T. S. 2007, *ApJ*, 663, 560
- Mark, J. W-K. 1968, *ApJ*, 154, 627
- Malkov, O. Yu. 1993, *Bull. Inf. CDS*, 42, 27
- Malkov, O. Yu. 2003, *A&A*, 402, 1055
- Malkov, O. Yu. 2007, *MNRAS*, 382, 1073
- Martin, P. G. 1970, *Ap&SS*, 7, 119
- McNally, D. 1965, *The Observatory*, 85, 166
- Meynet, G., & Maeder, A. 1997, *A&A*, 321, 465
- Mohan, C., Lal, A. K., Singh, V. P. 1992, *Ap&SS*, 193, 69
- Mohan, C., Lal, A. K., & Singh, V. P. 1997, *Ap&SS*, 254, 97
- Mohan, C., & Saxena, R. M. 1983, *Ap&SS*, 95, 369
- Mohan, C., Saxena, R. M., & Agarwal, S. R., 1990, *Ap&SS*163, 23
- Mohan, C., & Singh, V. P. 1978, *Ap&SS*54, 293
- Monaghan, F. F., & Roxburgh, I. W. 1965, *MNRAS*, 131, 13
- Motl, P. M., Frank, J., Tohline, J. E., & D'Souza, M. C. R. 2007, *ApJ*, 670, 1314
- Murray, C. D., & Dermott, S. F. 1999, *Solar System Dynamics* (Cambridge: Cambridge Univ. Press) 264
- Naylor, M. D. T., & Anand, S. P. S. 1972a, *Ap&SS*, 16, 137

- Naylor, M. D. T., & Anand, S. P. S. 1972b, *Ap&SS*, 18, 59
- Ostriker, J. P., & Mark, J. W-K. 1968, *ApJ*, 151, 1075
- Ostriker, J. P., & Bodenheimer, P. 1968, *ApJ*, 151, 1089
- Paczyński, B. 1971, *ARA&A*, 9, 183
- Paczyński, B. 1976, *IAU Symposium 73, Structure and Evolution of Close Binary Systems*, ed. P. Eggleton, S. Mitton, & J. Whelan (Reidel: Dordrecht), 75
- Pasinetti-Fracassini, L. E., Pastori, L., Covino, S., & Pozzi, A. 2001, *A&A*, 367, 521
- Press, W. H., Teukolsky, S. A., Vetterling, W. T., & Flannery, B. P. 1988, *Numerical Recipes in C*, 2nd ed. (Cambridge: Cambridge Univ. Press)
- Quataert, E. J., Kumar, P., & Ao, C. O. 1996, *ApJ*, 463, 284
- Rappaport, S., Joss, P. C., & Webbink, R. F. 1982, *ApJ*, 254, 616
- Ribas, I. 2006, *A&AS*, 304, 89
- Russell, H. N. 1928, *MNRAS*, 88, 641
- Schwarzschild, M. 1958, *Structure and Evolution of the Stars* (Princeton: Princeton Univ. Press)
- Singh, M., & Singh, G. 1983, *Ap&SS*, 96, 313
- Singh, M., & Singh, G. 1984, *Ap&SS*, 106, 161
- Stahler, S. W. 1983a, *ApJ*, 268, 155
- Stahler, S. W. 1983b, *ApJ*, 268, 165
- Stern, T. E., 1939, *MNRAS*, 99, 451
- Stothers, R. 1974, *ApJ*, 194, 651
- Smeyers, P., & Willems, B. 2001, *A&A*, 373, 173
- Tassoul, J. L. 1987, *ApJ*, 332, 856
- Tassoul, J. L. 1988, *ApJ*, 324, L71
- Torres, G., Lacy, C. H., Marschall, L. A., Sheets, H. A., & Mader, J. A. 2006, *ApJ*, 640, 1018
- Townsend, R. H. D., Owocki, S. P., & Howarth, I. D. 2005, *MNRAS*, 350, 189
- Weinberg, M. D. 1999, *AJ*, 117, 629

Wolff, S. C., Strom, S. E., Dror, D., Lanz, L., & Venn, K. 2006, *AJ*, 132, 749

Zahn, J. P. 1977, *A&A*, 57, 383

Table 1. Parameters of undisturbed polytropes

n	ξ_1	$\rho_c/\bar{\rho}$	N_n	I
0.5	2.7527	1.8352	2.5235	117.575
1.0	3.1416	3.2899	0.6366	101.844
1.5	3.6538	5.9907	0.4242	93.156
2.0	4.3529	11.4025	0.3648	88.895
2.5	5.3553	23.4065	0.3515	88.190
3.0	6.8969	54.1825	0.3639	90.910
3.5	9.5358	152.8837	0.4010	98.398
4.0	14.972	622.4079	0.4772	114.275
4.5	31.837	6189.4719	0.6580	152.617

Note. — n : polytropic index; ξ_1 : dimensionless volume radius; $\rho_c/\bar{\rho}$: central density concentration; N_n : coefficient of the mass-radius relation; I : dimensionless moment of inertia

Table 2. Parameters of uniformly-rotating polytropes in critical configuration

n	v_c	λ_c	N_n	I	$\rho_c/\bar{\rho}$	ξ_1	ξ_p	ξ_e
0.5	1.4409×10^{-1}	0.29386	1.42922	587.284	2.0394	3.4754	2.1779	4.8489
1.0	8.3880×10^{-2}	0.33967	0.45025	236.366	4.0494	3.7367	2.6922	4.8278
1.5	4.3622×10^{-2}	0.35168	0.34330	153.088	8.0619	4.2676	3.2962	5.3526
2.0	2.1576×10^{-2}	0.35694	0.32178	120.783	16.5434	5.0863	4.0556	6.2961
2.5	9.9305×10^{-3}	0.35922	0.32965	106.637	36.1737	6.3014	5.1000	7.7549
3.0	4.0803×10^{-3}	0.36019	0.35728	102.111	88.2755	8.1907	6.6738	10.0548
3.5	1.3861×10^{-3}	0.36057	0.40779	105.249	260.1278	11.4334	9.3419	14.0214
4.0	3.2913×10^{-4}	0.36071	0.49864	118.369	1095.9536	18.1078	14.8100	22.1991
4.5	3.2295×10^{-5}	0.36074	0.70213	154.862	11170.2095	38.7737	31.7202	47.5299

Note. — n : polytropic index; v_c & λ_c : critical values of the rotation parameters; N_n : coefficient of the mass-radius relation; I : dimensionless moment of inertia; $\rho_c/\bar{\rho}$: central density concentration; ξ_1 , ξ_p , & ξ_e : dimensionless volume, polar, and equatorial radii, respectively

Table 3. Fitting coefficients for the various parameters of rotating polytropes

f	$n = 1.5$					$n = 3$				
	a_0	a_1	a_2	a_3	a_4	a_0	a_1	a_2	a_3	a_4
ξ_1	3.65375	0.03588	0.00452	-0.11724	0.21911	6.89685	0.30538	0.18974	-0.24088	0.96237
ξ_c	3.65375	0.06834	0.01192	-0.25324	0.22619	6.89685	0.40291	0.47814	-0.45359	0.99175
ξ_p	3.65375	-0.07555	-0.00142	0	0	6.89685	-0.22243	-0.00057	0	0
$\rho_c/\bar{\rho}$	5.99070	0.01990	0.01092	-0.52212	0.22119	54.18248	3.83480	4.55374	-7.62154	0.96447
N_n	0.42422	-0.00904	-0.00057	0.00996	0.21821	0.36394	-0.00599	-0.00066	0	0
I	93.15635	2.05830	0.25902	-30.87279	0.17755	90.90975	8.53385	2.62075	0	0

Note. — a_i 's are defined through equation (34).

Table 4. Fitting coefficients for $\rho_c/\bar{\rho}$ of distorted polytropes

μ	$n = 1.5, b_0 = 5.99070$				$n = 3, b_0 = 54.18248$			
	b_1	b_2	b_3	b_4	b_1	b_2	b_3	b_4
0.1	-0.17092	3.49535	0.06614	28.20734	-2.46052	59.12506	9.44135	17.55872
0.2	-0.12860	2.13006	0.03425	21.79792	-1.85425	36.09363	5.38216	13.12862
0.3	-0.10830	1.58568	0.02566	18.13797	-1.55648	26.79729	4.29253	10.56543
0.4	-0.09552	1.28070	0.02340	15.36396	-1.36230	21.48995	4.03468	8.63850
0.5	-0.08637	1.08067	0.02478	12.96732	-1.21555	17.90157	4.23624	7.02247
0.6	-0.07921	0.93547	0.03011	10.74527	-1.09285	15.18838	4.84080	5.60038
0.7	-0.07320	0.82138	0.04173	8.62004	-0.98314	12.95893	5.89126	4.33881
0.8	-0.06148	0.68295	0.08494	6.11931	-0.88629	11.05241	7.38448	3.25984
0.9	-0.06648	0.65962	0.09659	4.98583	-0.83960	9.68781	8.75499	2.46508

Note. — b_i 's are defined through equation (38).

Table 5. Fitting coefficients for the volume radius ξ_1 of distorted polytropes

μ	$n = 1.5, b_0 = 3.65375$				$n = 3, b_0 = 6.89685$			
	b_1	b_2	b_3	b_4	b_1	b_2	b_3	b_4
0.1	-0.05174	1.22025	0.13999	19.60622	-0.10449	2.60661	0.64437	15.45073
0.2	-0.03954	0.75031	0.07579	14.87539	-0.07951	1.59668	0.36468	11.50900
0.3	-0.03346	0.56039	0.05810	12.14228	-0.06669	1.18356	0.29108	9.18447
0.4	-0.02956	0.45272	0.05287	10.08102	-0.05814	0.94518	0.27414	7.41921
0.5	-0.02668	0.38076	0.05430	8.32835	-0.05149	0.78149	0.28845	5.93073
0.6	-0.02434	0.32725	0.06149	6.75355	-0.04571	0.65486	0.33023	4.61883
0.7	-0.02233	0.28415	0.07542	5.31595	-0.04026	0.54723	0.40290	3.45588
0.8	-0.01862	0.23208	0.11519	3.75473	-0.03496	0.44995	0.50912	2.45910
0.9	-0.02015	0.22374	0.11821	3.07080	-0.03043	0.36682	0.62743	1.69514

Note. — b_i 's are defined through equation (38).

Table 6. Fitting coefficients for N_n of distorted polytropes

μ	$n = 1.5, b_0 = 0.42422$				$n = 3, b_0 = 0.36394$			
	b_1	b_2	b_3	b_4	b_1	b_2	b_3	b_4
0.1	0.00696	-0.18218	-0.06256	14.81447	0.00110	-0.06453	1.14963	-11.8357
0.2	0.00533	-0.11239	-0.03379	11.12954	0.00086	-0.03997	0.56067	-9.41496
0.3	0.00452	-0.08394	-0.02569	8.96846	0.00075	-0.03009	0.36519	-8.22768
0.4	0.00399	-0.06755	-0.02301	7.32661	0.00068	-0.02458	0.26786	-7.45925
0.5	0.00357	-0.05633	-0.02307	5.92820	0.00064	-0.02104	0.20972	-6.89082
0.6	0.00321	-0.04771	-0.02524	4.67990	0.00061	-0.01856	0.17112	-6.43430
0.7	0.00288	-0.04047	-0.02957	3.55301	0.00059	-0.01675	0.14367	-6.04829
0.8	0.00229	-0.03146	-0.04086	2.37704	0.00058	-0.01534	0.12333	-5.72063
0.9	0.00238	-0.02892	-0.04344	1.78659	0.00055	-0.01410	0.10903	-5.50715

Note. — b_i 's are defined through equation (38).

Table 7. Fitting coefficients for I of distorted polytropes

μ	$n = 1.5, b_0 = 90.91016$				$n = 3, b_0 = 93.15765$			
	b_1	b_2	b_3	b_4	b_1	b_2	b_3	b_4
0.1	0.23389	-6.78106	416.21309	0.06683	-4.44876	133.13261	152.14256	10.18132
0.2	0.13995	-3.24888	197.05415	0.05320	-3.27895	78.57307	81.88516	7.48309
0.3	0.10835	-2.25890	127.38938	0.00015	-2.69940	56.50289	58.48508	6.01238
0.4	0.09711	-1.90272	93.74429	-0.06256	-2.32438	43.95814	47.13868	4.97229
0.5	0.09662	-1.80771	74.20831	-0.12872	-2.05058	35.62331	40.77503	4.14597
0.6	0.10447	-1.86636	61.68649	-0.19697	-1.83950	29.58690	36.91530	3.45368
0.7	0.12211	-2.06525	53.29763	-0.26863	-1.68084	25.05345	34.30903	2.86731
0.8	0.15798	-2.48941	47.93900	-0.35028	-1.48905	20.90588	33.51635	2.31784
0.9	0.25324	-3.60727	46.46436	-0.47006	-1.67258	20.43106	27.78674	2.09483

Note. — b_i 's are defined through equation (38)

Table 8. Fitting coefficients for ν_c of the critical components

	$n = 1.5$	$n = 3$
d_0	5.283	10.051
d_1	22.07	39.75
d_2	-87.99	-155.79
d_3	236.69	420.65
d_4	-292.31	-522.14
d_5	141.03	253.75
e_0	1.101	2.242
e_1	7.922	14.798

Note. — d_i 's and e_i 's are defined through equation (45).

Table 9. Fitting coefficients for $\Delta \log k_{2,\text{eff}}$

μ	n=1.5			n=3			n=3.5		
	a_1	a_2	a_3	a_1	a_2	a_3	a_1	a_2	a_3
0.1	0.73385	34.10425	-148.77090	-0.03012	24.47968	-196.59523	-0.08969	21.17797	-182.98519
0.2	0.88514	30.49465	-120.51368	0.12028	21.15117	-167.29413	0.07023	16.73734	-137.84158
0.3	1.00745	25.75547	-87.11816	0.23724	17.77352	-135.98160	0.17016	14.06672	-113.16240
0.4	1.05899	23.41619	-91.19969	0.32678	14.69585	-107.93152	0.24079	11.91660	-93.63182
0.5	1.16935	15.72668	-29.29898	0.41656	10.91861	-74.44114	0.29680	10.04001	-79.29394
0.6	1.19753	11.16234	-9.88845	0.48402	7.43452	-45.76199	0.39296	5.57693	-38.07912
0.7	1.15145	8.27121	-8.49183	0.52890	4.11300	-21.09957	0.42220	3.49667	-23.59086
0.8	1.04939	4.77987	1.27992	0.52238	1.64450	-5.99889	0.44813	0.61004	-3.06641
0.9	0.79149	2.31621	4.14140	0.40330	0.52695	-1.00724	0.34866	-0.12201	0.77103
1.0	0.10778	1.67357	-2.14200	0.04236	0.43492	-0.71212	0.03456	0.28929	-0.54041

Note. — a_i 's are defined through equation (50).

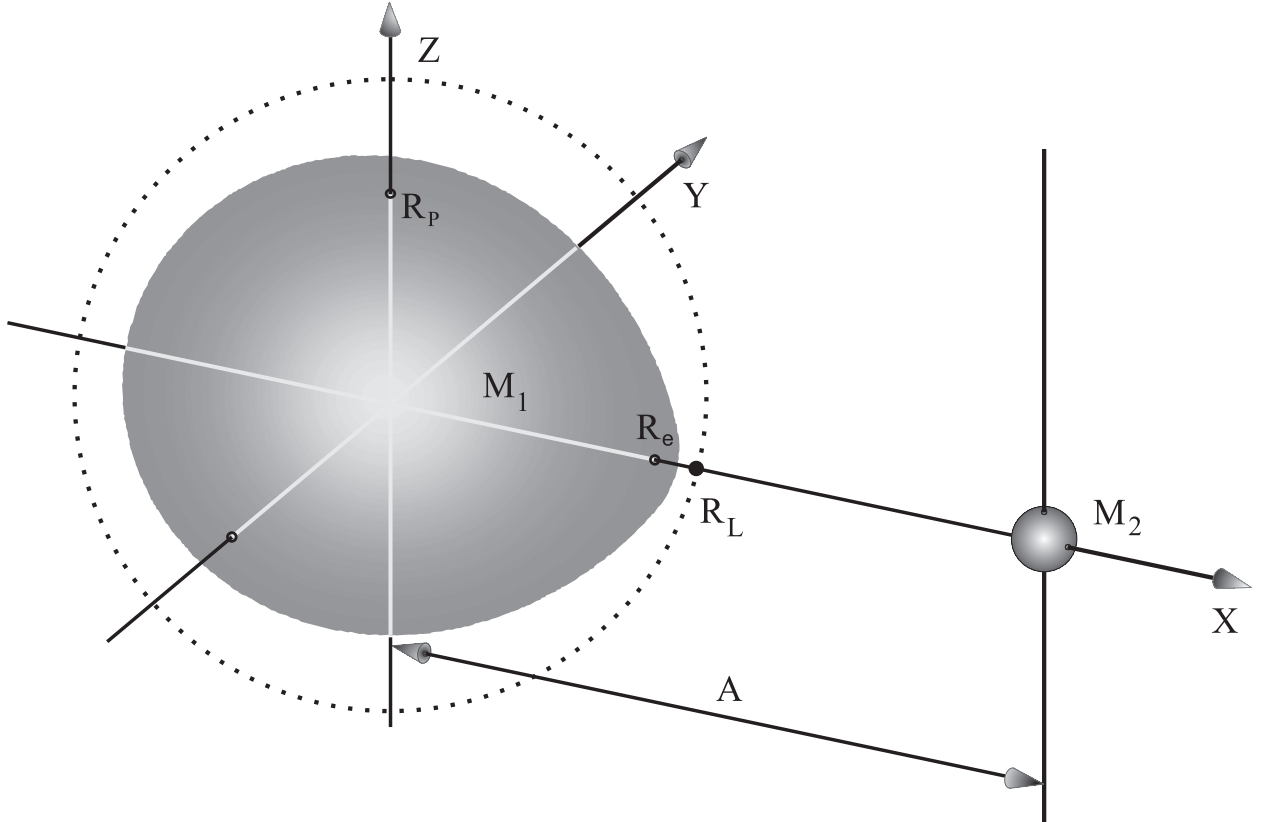


Fig. 1.— Schematic view of a binary configuration consisting of a distorted polytrope (star I) with mass M_1 and its point-mass companion (star II) with mass M_2 . The Cartesian coordinate system (x, y, z) corotating with the binary is centered at the center of mass of star I that has polar and equatorial radii R_p and R_e in the z - and positive x -directions, respectively. Star II is located at $(A, 0, 0)$. Dotted line draws a sphere with radius equal to the distance from the center of mass of star I to the Lagrange point R_L of the binary.

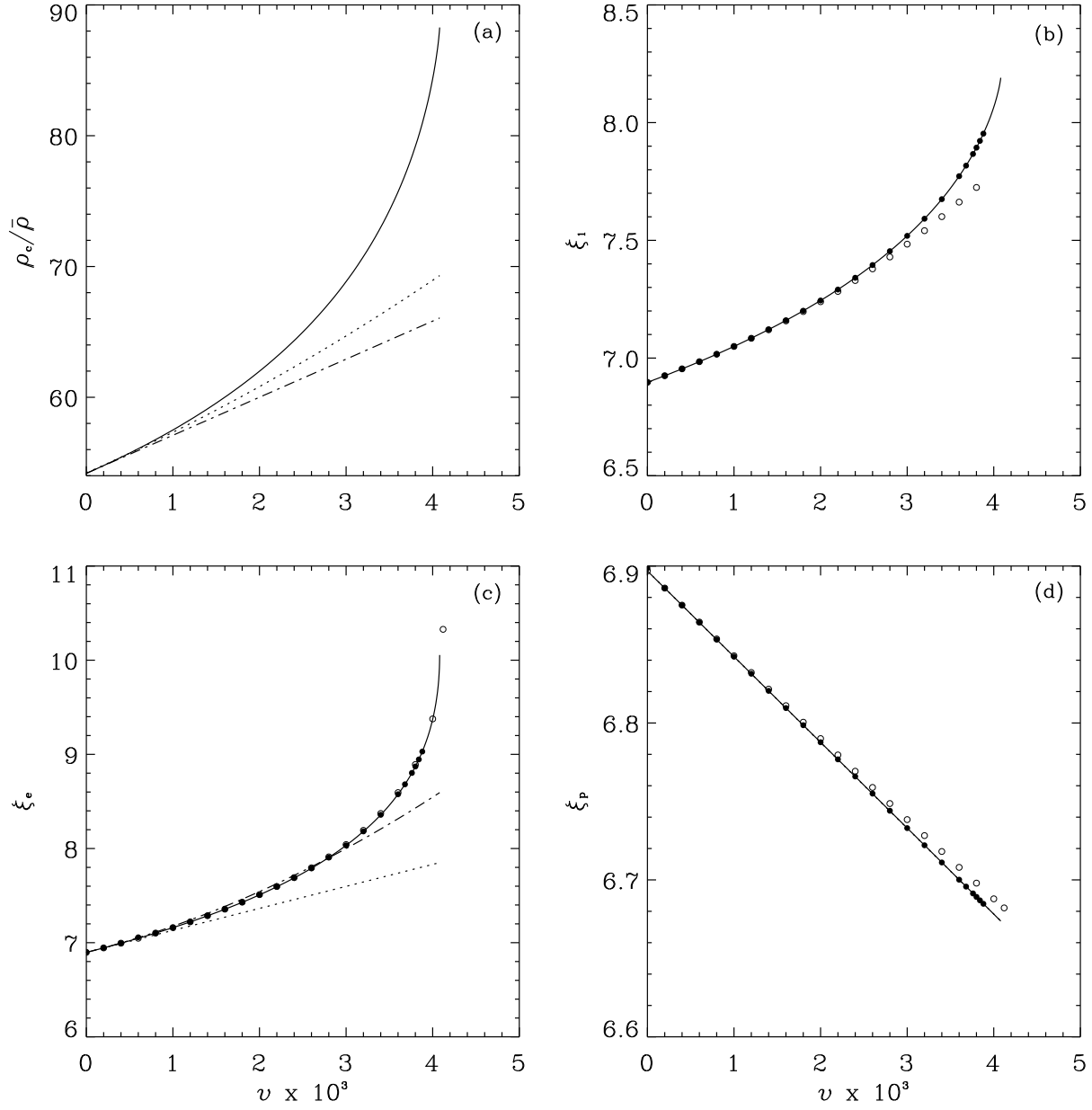


Fig. 2.— Dependences on the rotation parameter v of (a) the mass concentration $\rho_c/\bar{\rho}$, (b) volume radius ξ_1 , (c) equatorial radius ξ_e , and (d) polar radius ξ_p for rotating polytropes with $n = 3$. Solid lines plot the results of the present study, while dotted and dot-dashed lines are for the first- and second-order perturbation analyses of Chandrasekhar (1933a) and Anand (1968), respectively. Open circles denote the values from the advanced perturbation theory of Linnell (1977, 1981), while the direct numerical results of James (1964) are given by filled circles.

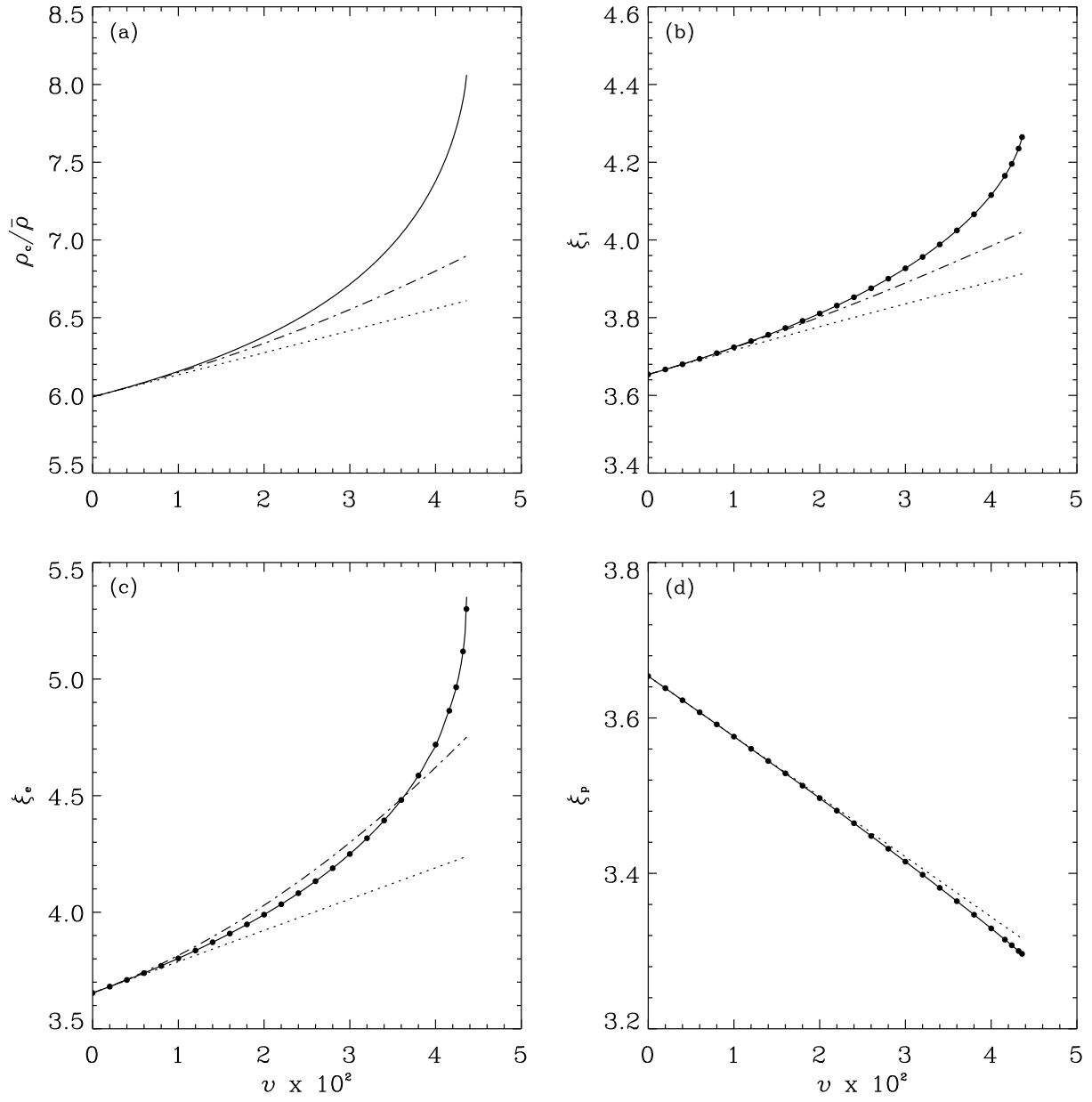


Fig. 3.— Same as Figure 2 except for $n = 1.5$ polytropes.

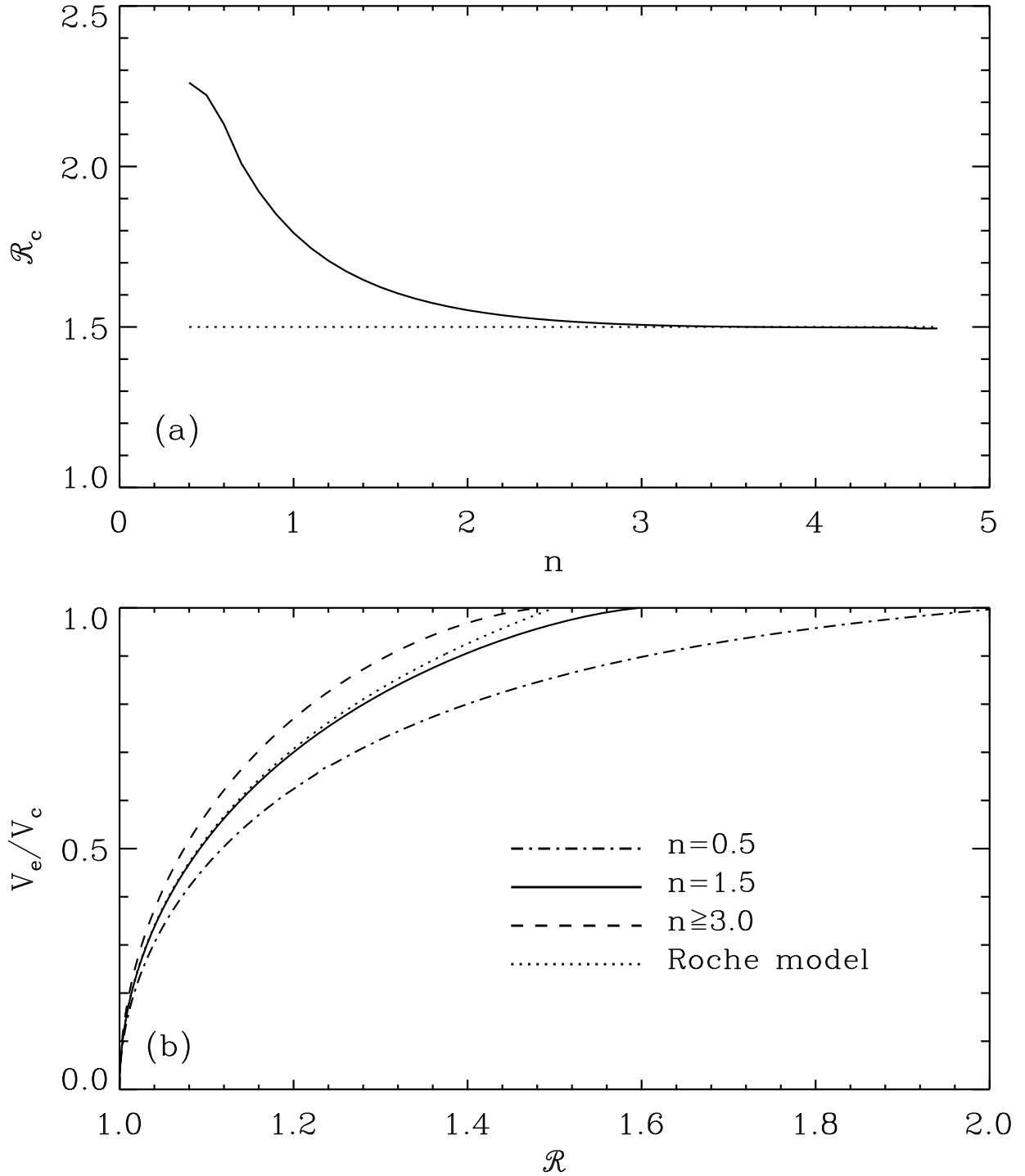


Fig. 4.— *a*: Critical values of the aspect ratio $\mathcal{R} = \xi_e/\xi_p$ resulting from our self-consistent solutions for rotating polytropes with index n (*solid line*) and the prediction, $\mathcal{R}_c = 1.5$, of the Roche models (*dotted line*). *b*: Dependence on \mathcal{R} of the ratio V_e/V_c of the equatorial to critical velocities. Curves for $n \geq 3.0$ are almost indistinguishable.

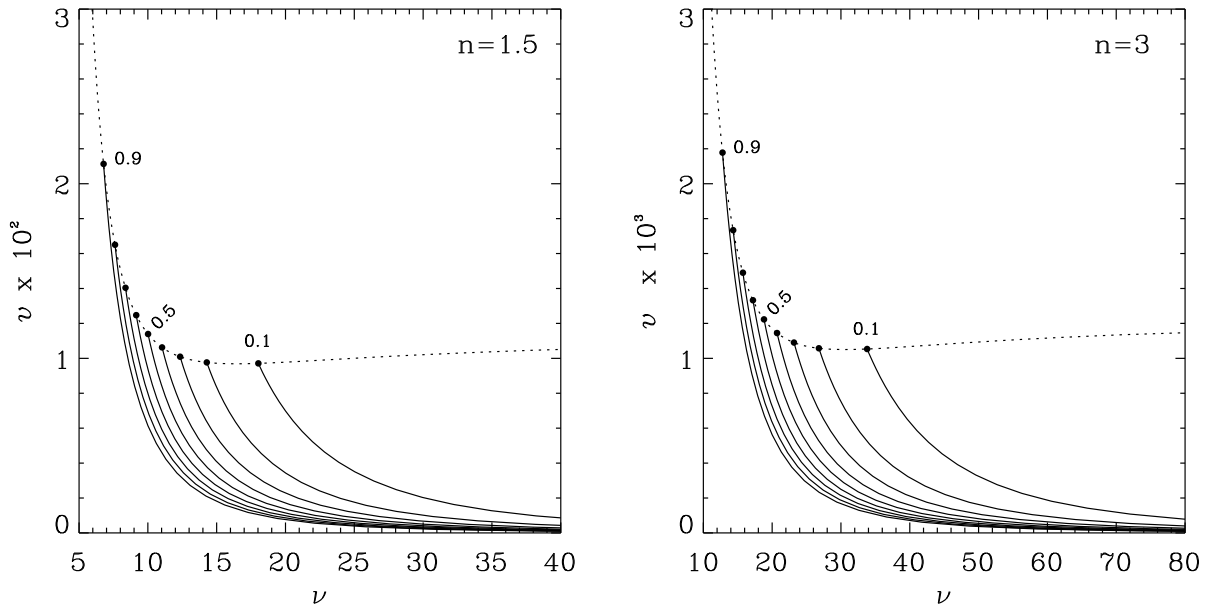


Fig. 5.— Dependences of the rotation parameter v on the dimensionless orbital separation ν for self-consistent equilibrium polytropes with (*left*) $n = 1.5$ and (*right*) $n = 3$ under both rotational and tidal perturbations. Each solid line corresponds to a sequence of equilibrium polytropes with fixed relative mass μ indicated at one end of the line. The critical configuration at each sequence is marked by a filled circle. The dotted line connecting the filled circles demarcates the boundary in the ν - v plane above which no equilibrium polytrope exists.

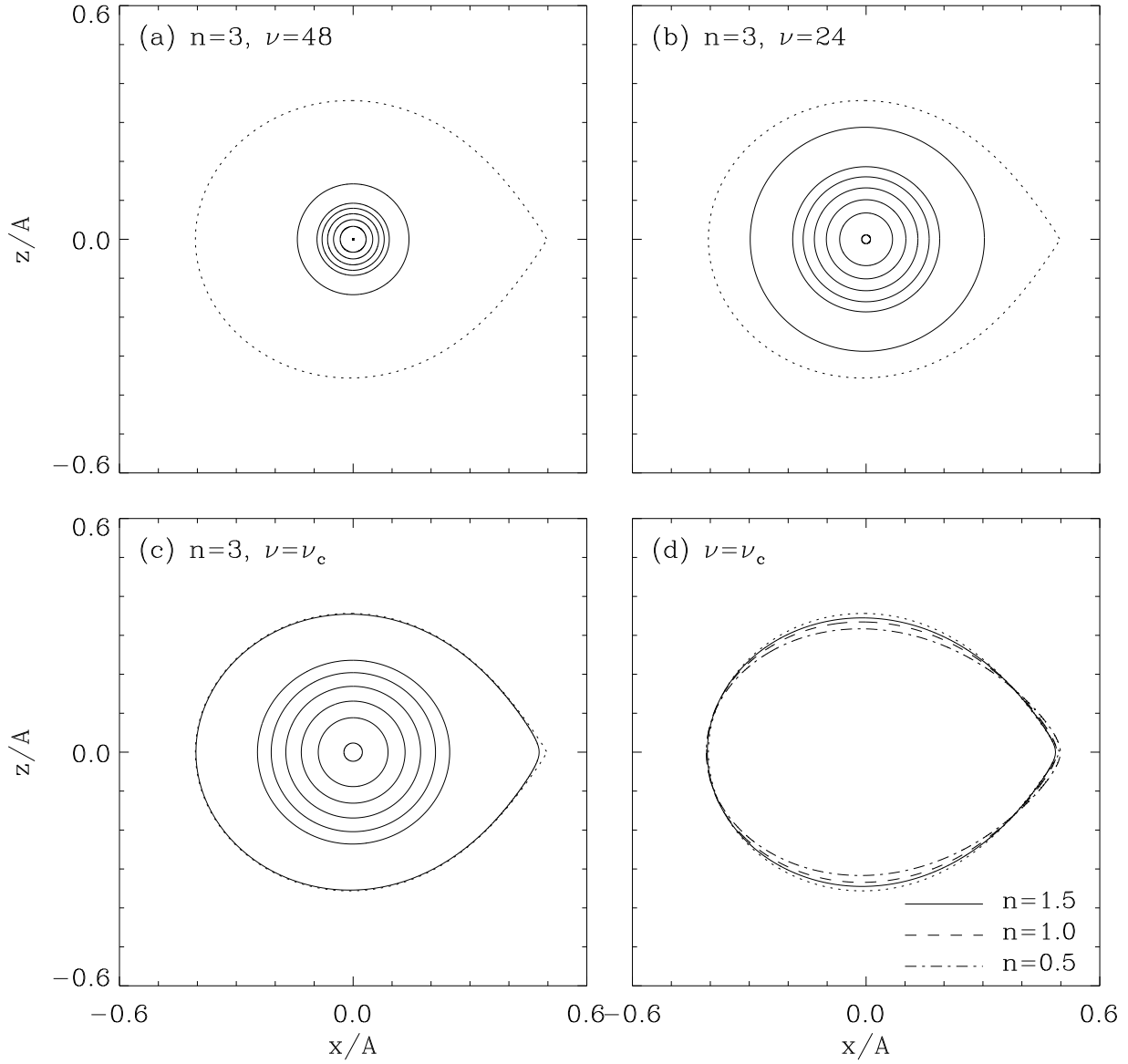


Fig. 6.— *a-c*: Meridional cross-sections of constant density surfaces of distorted equilibrium polytropes with $n = 3$. Solid contours correspond to $\rho/\bar{\rho} = 3^{-m}(\rho_c/\bar{\rho})_{\text{iso}}$ with $m = 0, 1, \dots, 5, \infty$ from inside to outside. *d*: Outer boundaries of the distorted polytropes in critical configuration. In all the panels, the dotted line draws the Roche lobe around star I that has a half of the total mass ($\mu = 0.5$). See text for details.

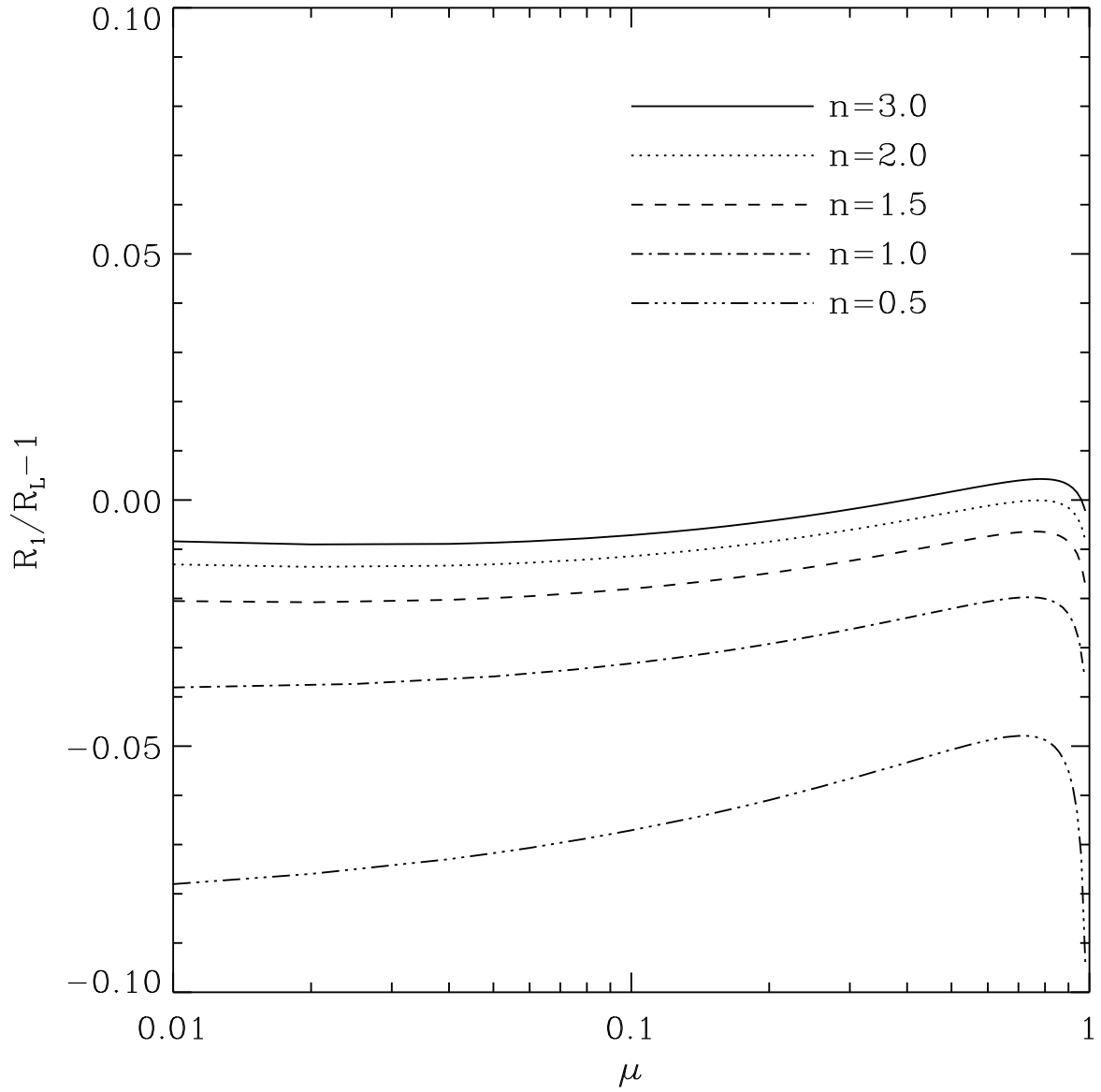


Fig. 7.— Comparison of the volume radius R_1 of a critical component with the effective radius R_L of the corresponding Roche model.

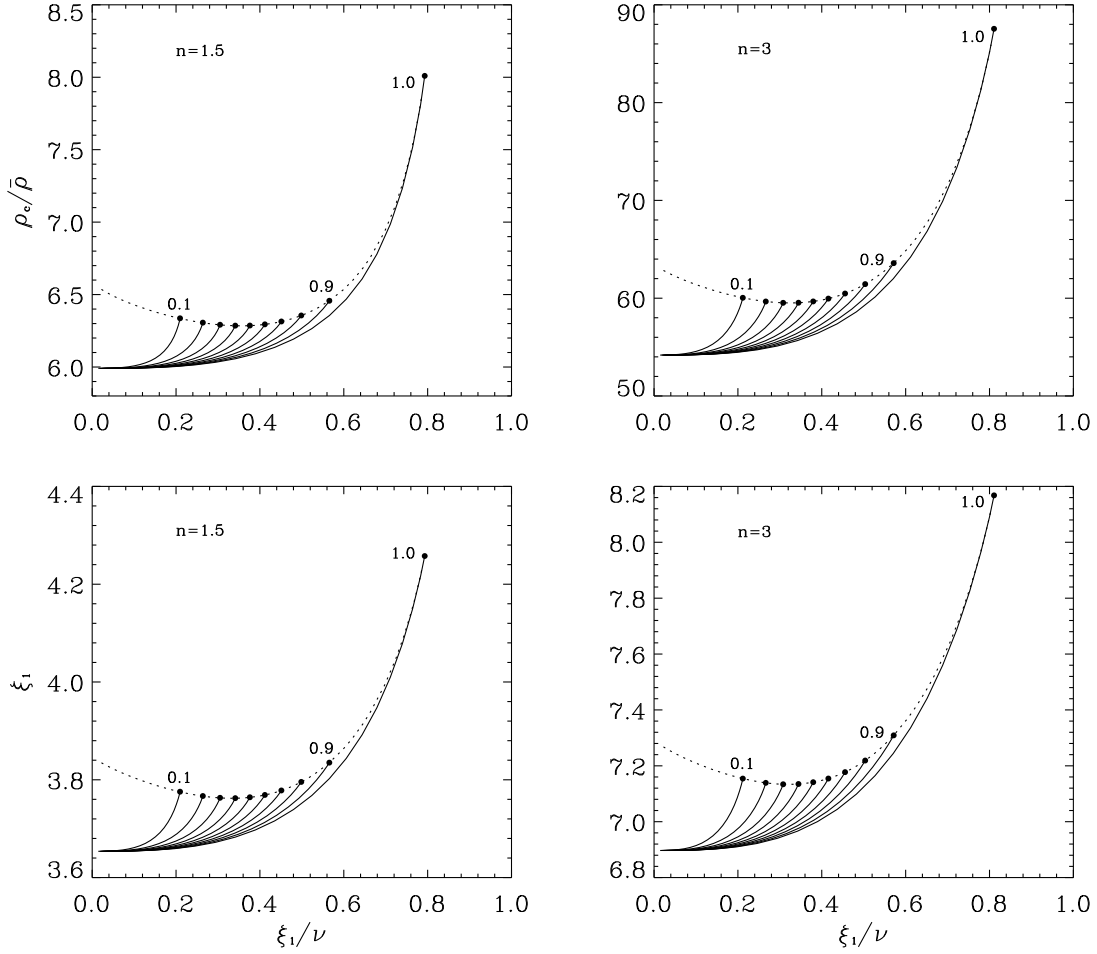


Fig. 8.— Dependences of $\rho_c/\bar{\rho}$ and ξ_1 on the relative radius $R_1/A = \xi_1/\nu$ for (*left*) $n = 1.5$ and (*right*) $n = 3.0$ polytropes. Each solid line is a sequence of distorted polytropes with fixed relative mass μ indicated at one end of the line. The dotted lines connecting the filled circles, denoting the end points of the sequences, correspond to the critical components.

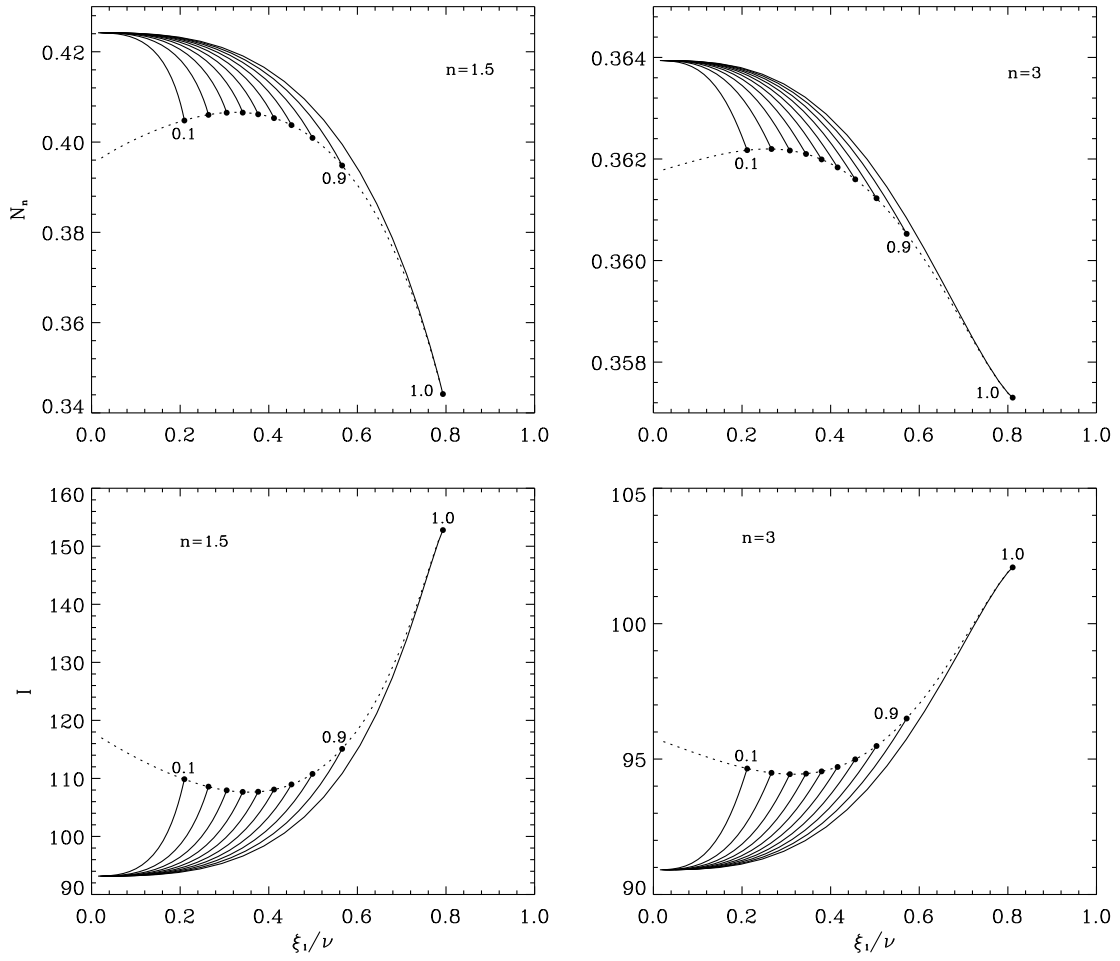


Fig. 9.— Same as Figure 8 for N_n and I .

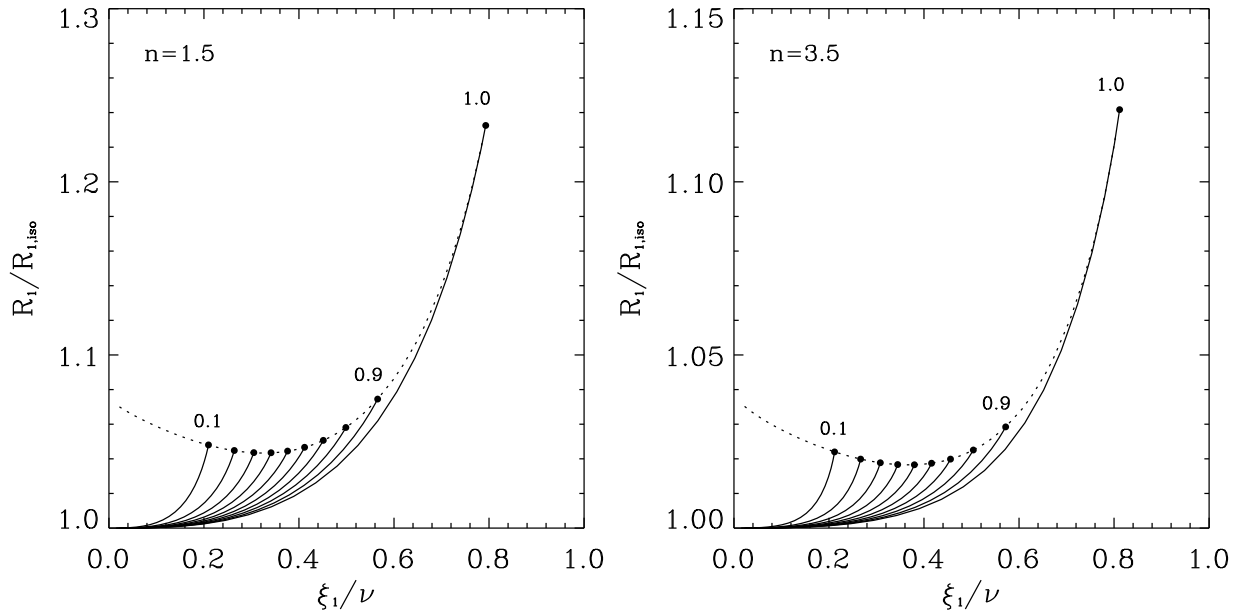


Fig. 10.— Changes in the radius of a star with fixed mass due to tidal and rotational perturbations under the assumption of constant pressure constant K for (*left*) $n = 1.5$ and (*right*) $n = 3.5$ polytropes. Each solid line is a sequence of distorted polytropes with fixed relative mass μ indicated at one end of the line. The dotted lines correspond to the critical components.

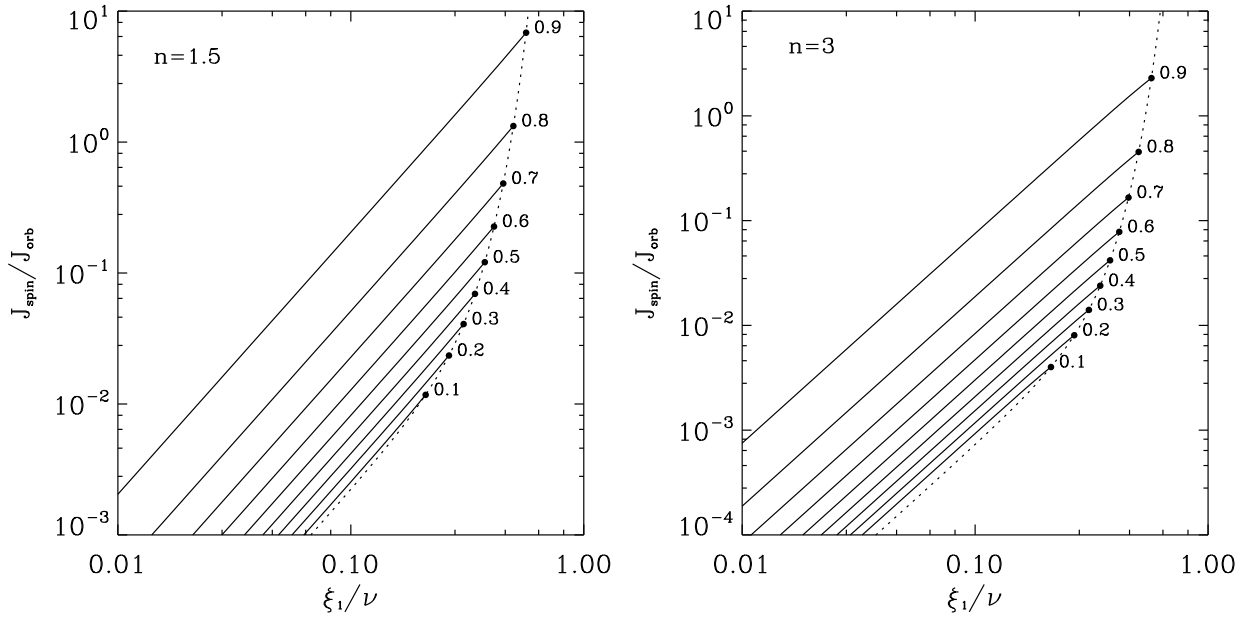


Fig. 11.— Ratio of the spin to orbital angular momenta, $J_{\text{spin}}/J_{\text{orb}}$, of (left) $n = 1.5$ and (right) $n = 3.0$ polytropes, as functions of ξ_1/ν and μ . Each solid line corresponds to a sequence of distorted polytropes with fixed relative mass μ indicated at one end of the line. The dotted lines connecting the filled circles, denoting the end points of the sequences, represent the critical components.

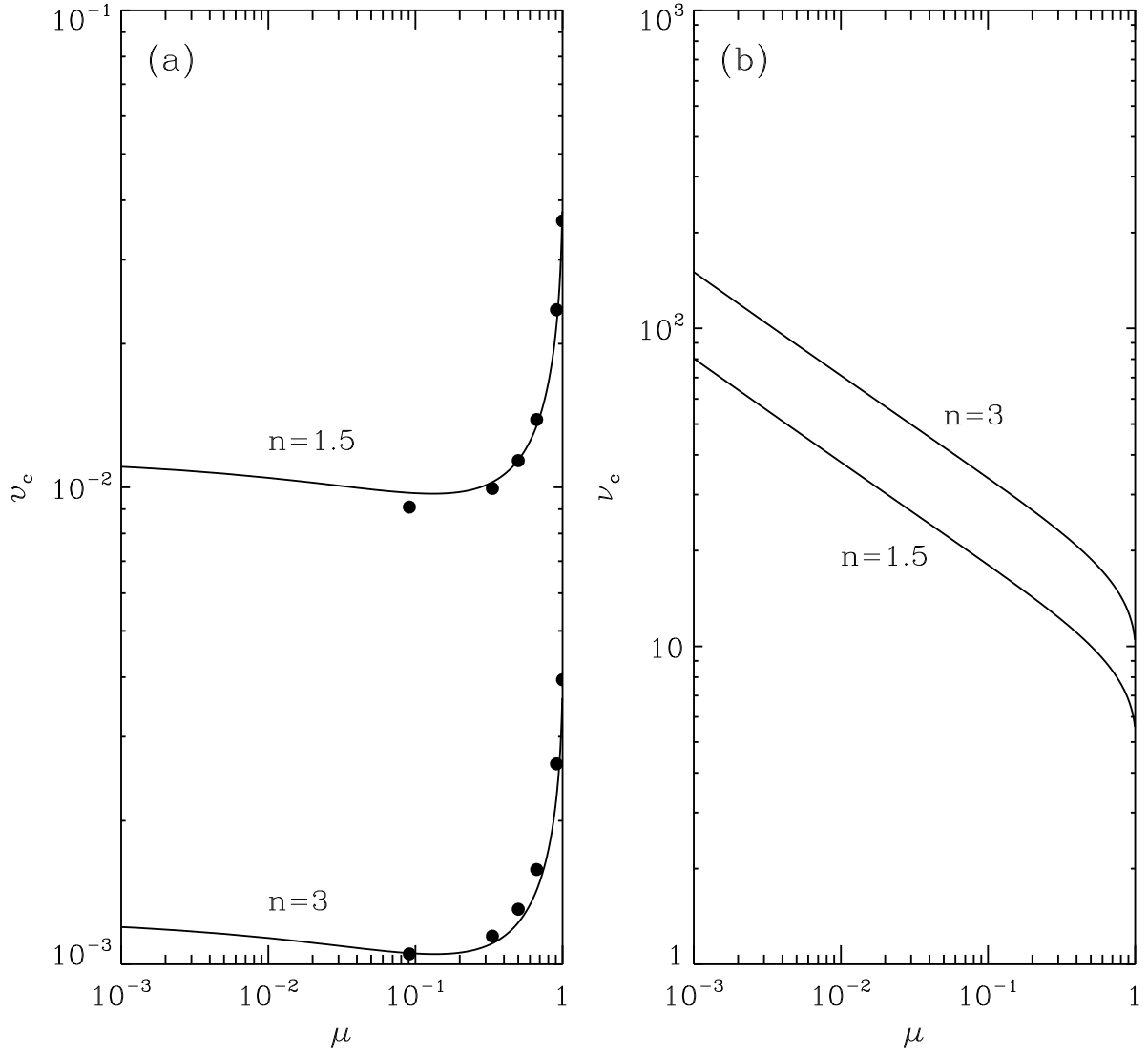


Fig. 12.— Dependences on μ of (a) the critical rotation parameter ν_c and (b) the critical dimensionless orbital separation ν_c for polytropes with $n = 1.5$ and 3.0 . In (a), the filled circles plots the results of Singh & Singh (1983) based on the double approximation method.

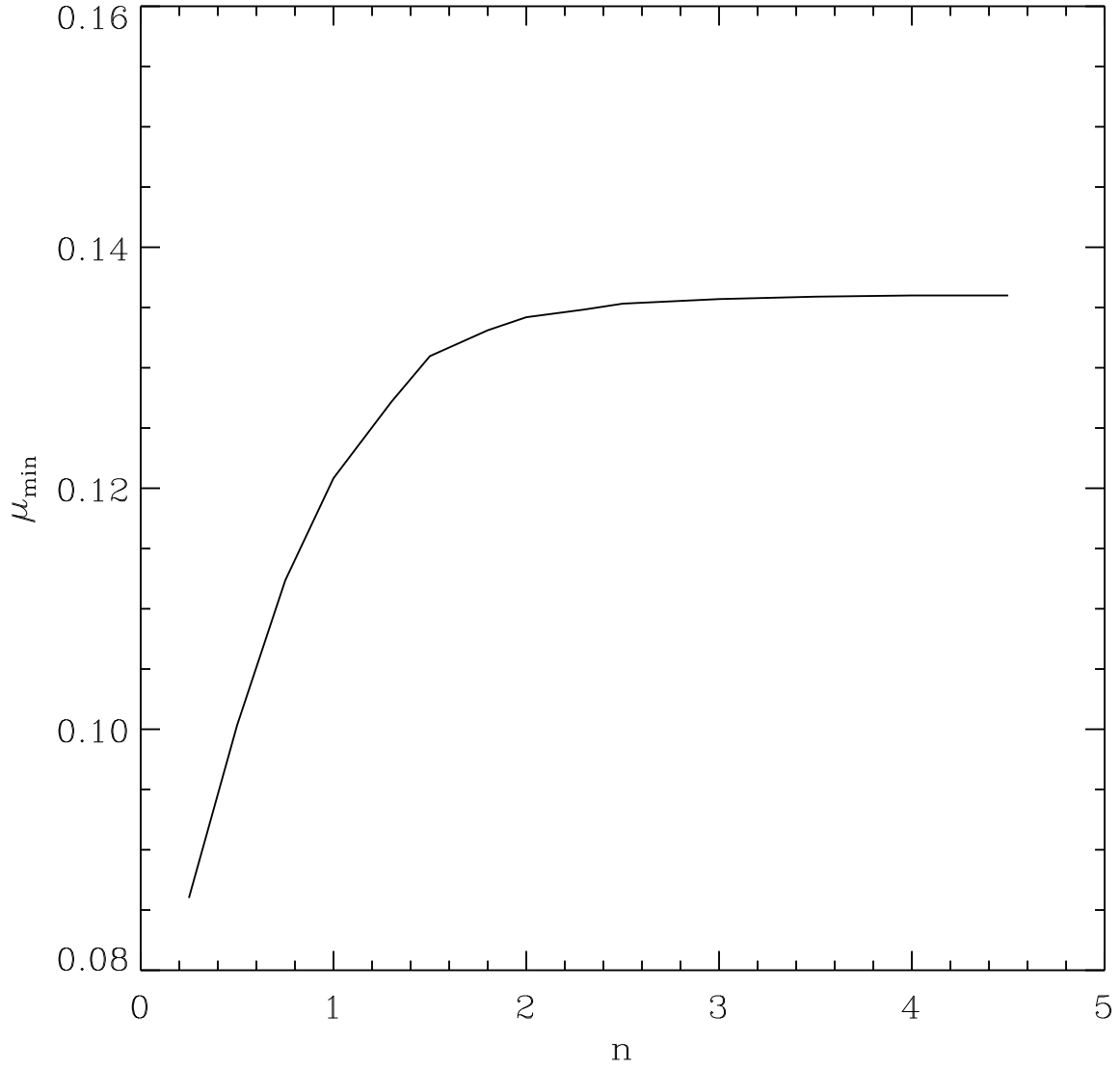


Fig. 13.— Dependence on n of μ_{\min} that minimize v_c . Note that $\mu_{\min} \rightarrow 0.136$ as $n \rightarrow 5$.

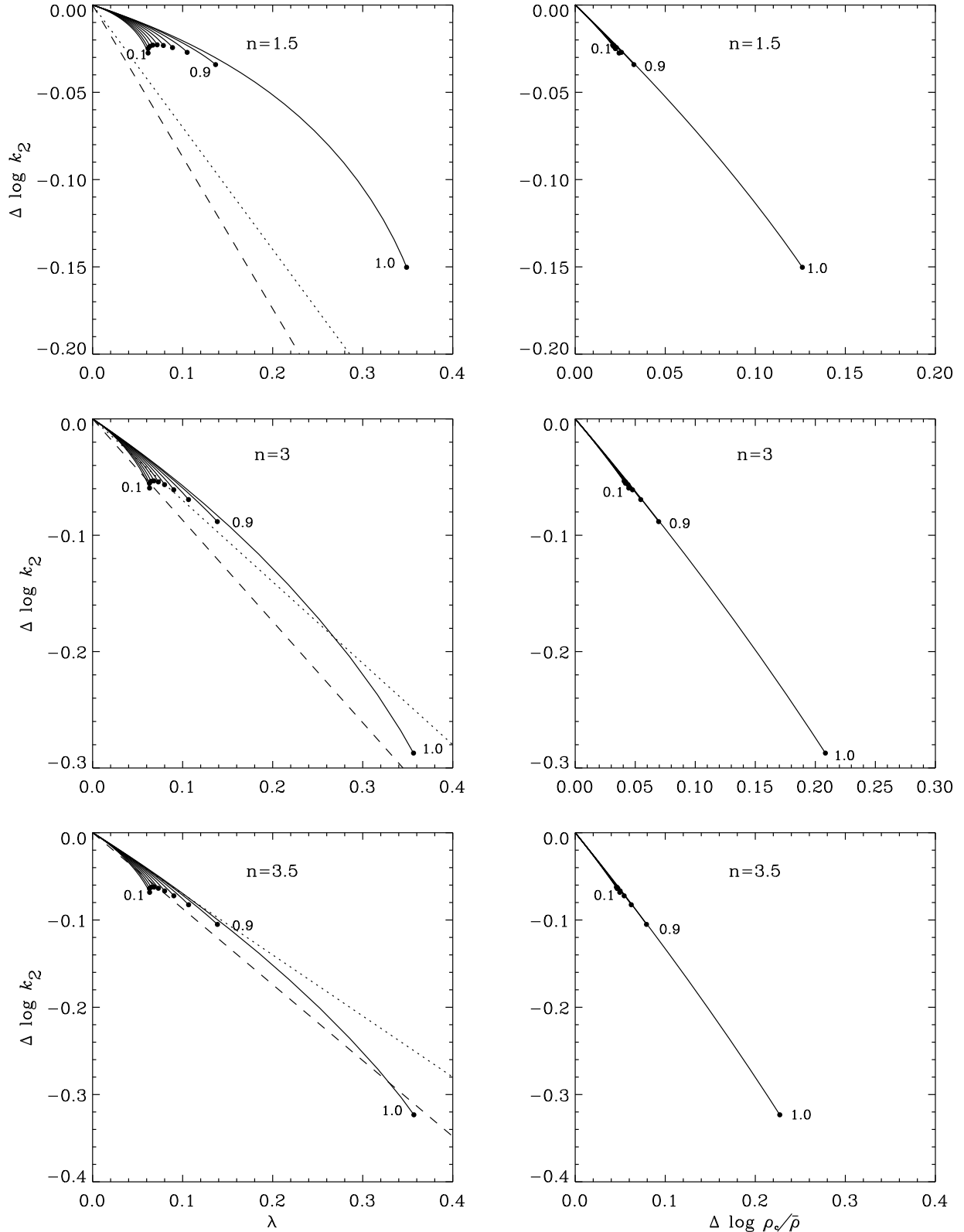


Fig. 14.— Variations of $\Delta \log k_2$ with (*left*) λ and (*right*) $\Delta \log \bar{\rho}/\rho_c$ for polytropes with $n = 1.5, 3.0$, and 3.5 . Each solid line is a sequence of distorted polytropes with fixed relative mass μ , with a filled circle at the tip of the line corresponding to a critical component. For comparison, $\Delta \log k_2 = -0.7\lambda$ and -0.87λ , the results of Stothers (1974) and Claret (1999) for rotationally-disturbed stars, are plotted as dotted and dashed lines, respectively.

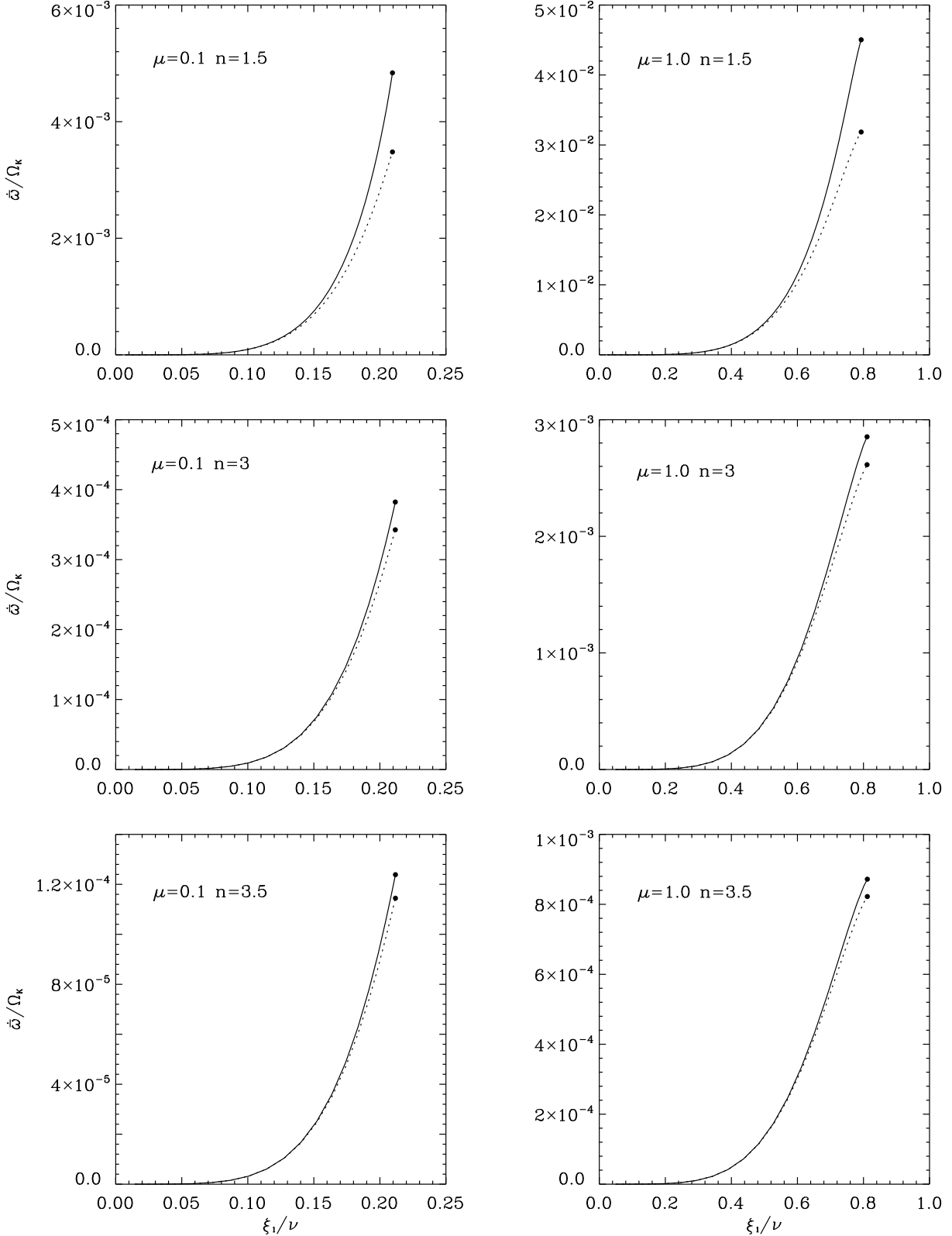


Fig. 15.— Apsidal motion rate $\dot{\omega}$ versus the relative radius ξ_1/ν for cases with (left) $\mu = 0.1$ and (right) $\mu = 1.0$. Solid lines plot $\dot{\omega}_n$ calculated from our self-consistent solutions for distorted polytropes, while dotted lines are for the theoretical rates $\dot{\omega}_t$ based on the first-order perturbation method, with k_2 calculated for distorted polytropes from the Radau equation. For sufficiently large ξ_1/ν , $\dot{\omega}_n$ is larger than $\dot{\omega}_t$.

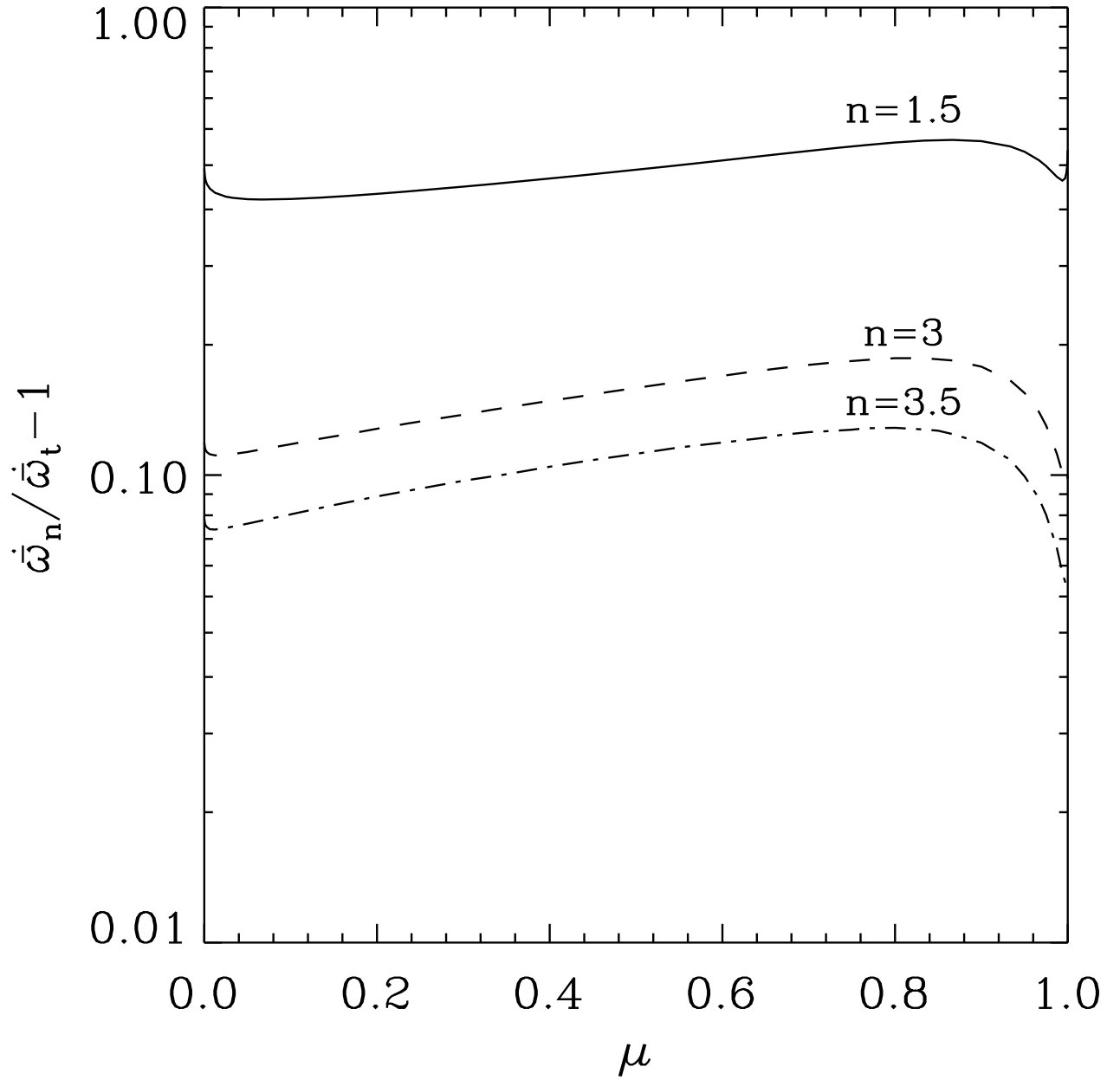


Fig. 16.— Relative difference between the numerical and theoretical apsidal motion rates, $\dot{\omega}_n$ and $\dot{\omega}_t$, against the relative mass μ for critical components.

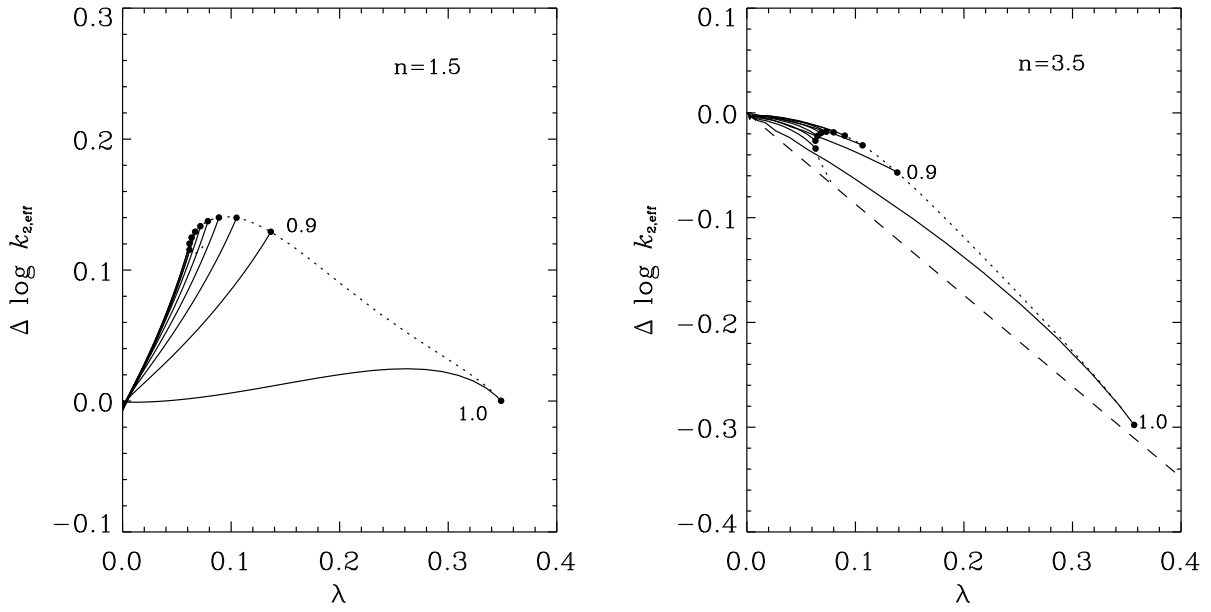


Fig. 17.— Dependence of $\Delta \log k_{2,\text{eff}}$ on the rotation parameter λ for (*left*) $n = 1.5$ and (*right*) $n = 3.5$ polytropes. Each solid line is a sequence of distorted polytropes with fixed relative mass μ . Dotted lines correspond to the critical components. The result, $\Delta \log k_{2,\text{eff}} = -0.87\lambda$, of Claret (1999) for rotationally-disturbed stars is drawn as a dashed line in the right panel.